

# Simulation-based cosmological inference from optically-selected galaxy clusters with Capi sh

Constantin Payerne<sup>1</sup>, Calum Murray<sup>1,2</sup>, Hugo Simon<sup>1</sup>

<sup>1</sup> Université Paris-Saclay, CEA, IRFU, 91191 Gif-sur-Yvette, France

<sup>2</sup> Université Paris Cité, CNRS-IN2P3, APC, 75013 Paris, France

Received September 15, 1996; accepted March 16, 1997

## ABSTRACT

Galaxy clusters are powerful probes of the growth of cosmic structure through measurements of their abundance as a function of mass and redshift. Extracting precise cosmological constraints from cluster surveys is challenging, as we must contend with non-trivial correlations between lensing mass and optical richness, as well as the complex relationship between richness and the underlying halo mass. These difficulties are compounded by systematic effects such as selection function biases, super-sample covariance, and correlated measurement noise between mass proxies. As upcoming photometric surveys are expected to detect tens to hundreds of thousands of galaxy clusters, controlling these systematics becomes essential. In this paper, we present a forward-modelling approach using Simulation-Based Inference (SBI), which provides a natural framework for jointly modelling cluster abundance and lensing mass observables while capturing systematic uncertainties at higher fidelity than analytic likelihood methods — which rely on simplifying assumptions such as fixed covariances and Gaussianity — without requiring an explicit likelihood formulation. We introduce Capi sh, a Python code for generating forward-modelled galaxy cluster catalogues using halo mass functions and incorporating observational effects. We perform SBI using neural density estimation with normalizing flows, trained on abundance and mean lensing mass measurements in observed redshift–richness bins. Key cluster-related summary statistics measured on Capi sh simulations faithfully reproduce their corresponding analytical predictions, and we perform several Bayesian robustness tests of the posterior modelling. Our forward model accounts for realistic noise, redshift uncertainties, selection functions, and correlated scatter between lensing mass and observed richness. We find good agreement with likelihood-based analyses, with broader SBI posteriors reflecting the increased realism of the forward model. We also test Capi sh on cluster catalogues built from a large cosmological simulation, finding a good fit to cosmological parameters.

**Key words.** Galaxies: clusters: general - Gravitational lensing: weak –methods: statistical

## 1. Introduction

Galaxy clusters form through the gravitational collapse of large matter density fluctuations and emerge as the largest gravitationally bound objects at the intersection of the cosmic web filaments. Therefore, their formation history, mass, and spatial distribution are highly connected to the fluctuations of the matter density field, the expansion rate of the Universe, and the nature of gravity (e.g., Bartlett 1997).

Constraining cosmological parameters through the abundance of galaxy clusters relies on connecting the observed cluster count to the underlying mass and redshift distribution of the most massive dark matter halos. Cluster masses are not directly observable. With optical surveys, clusters are detected through the density of their member galaxies (Rykoff et al. 2014), and each cluster is assigned a richness, which is linked to the number of cluster’s galaxy members. The constraining power of cluster number counts is currently limited by our understanding of the cluster scaling relations (Pratt et al. 2019), linking the underlying cluster mass and with what we observe.

Weak gravitational lensing (Bartelmann & Schneider 2001) has become a robust tool for constraining cluster masses (e.g., McClintock et al. 2019; Umetsu 2020; Murray et al. 2022; Mistele & Durakovic 2024; Grandis et al. 2024; Murray et al. 2025), through the coherent distortion of the shapes of background galaxy images, caused by the bending of the light path due to

the cluster’s gravitational field. When available, cluster lensing information has been crucial in tightening the constraints on the cluster mass–proxy relation (see e.g. von der Linden et al. 2014; Penna-Lima et al. 2017).

Over the past two decades, the measurement of the abundance of galaxy clusters has provided competitive constraints on  $\Omega_m$  and  $\sigma_8$ , from optically-detected clusters by the Dark Energy Survey<sup>1</sup> (DES, Abbott et al. 2020, 2025; To et al. 2021; Costanzi et al. 2021), the Kilo Degree Survey (KiDS, Lesci et al. 2022; Lesci et al. 2025), the Sloan Digital Sky Survey (SDSS, Fumagalli et al. 2023; Park et al. 2023; Sunayama et al. 2024), from X-ray-detected clusters by ROSAT (Mantz et al. 2015), eROSITA (Ghirardini et al. 2024) and from clusters detected through the Sunyaev-Zeldovich (SZ) effect at millimeter wavelengths by the Planck satellite (Ade et al. 2016; Zubeldia & Challinor 2019; Salvati et al. 2022; Lee et al. 2024; Aymerich et al. 2024), the South Pole Telescope (SPT, Chabul et al. 2022; Bocquet et al. 2024; Bocquet et al. 2025) or the Atacama Cosmology Telescope (ACT, Sehgal et al. 2011; Hasselfield et al. 2013). Large cluster surveys such as the Legacy Survey of Space and Time of the Vera Rubin Observatory (LSST Science Collaboration et al. 2009), the Euclid mission (Laureijs et al. 2011) will detect tens to hundreds of thousands of clusters and provide even stronger cosmological constraints.

<sup>1</sup> Although it should be noted that the Abbott et al. (2020) found a significant tension with the other DES analysis.

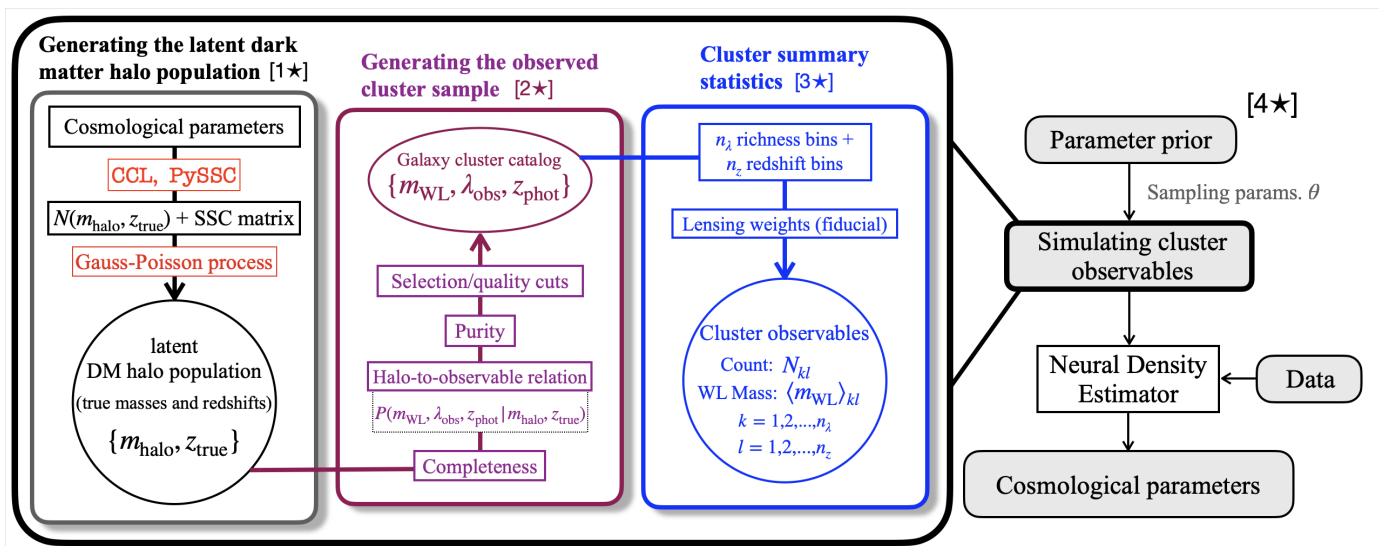


**Fig. 1.** Organization of Capi.sh, detailed in Section 2: The code is organized in three separate blocks: the first block [1★] is dedicated to generate halo masses and true redshift from an underlying halo mass function, accounting for the effect of SSC (presented in Section 2.1) The second block [2★] is dedicated to compute the observed richness and lensing mass for halos, along with photometric redshift (presented in Section 2.2). The third block [3★] computes the summary statistics (presented in Section 2.3). [4★] denotes for the overall SBI structure.

The cosmological constraining power of number counts of optically-selected clusters is limited by a range of systematic effects that must be understood and controlled. On the theoretical side, these include uncertainties in the modelling of the dark matter density profile in the cluster field (Becker & Kravtsov 2011; Lee et al. 2018) and in the calibration of the halo mass function (Artis et al. 2021). Cluster number counts also deviate from a simple Poisson process (Poisson 1837), as fluctuations in the underlying matter density field introduce additional correlated scatter known as Super-Sample Covariance (SSC; Hu & Kravtsov 2003; Gouyou Beauchamps et al. 2022), which constitutes an important source of variance for cluster count measurements (Fumagalli et al. 2021; Payerne et al. 2023, 2024). On the observational side, further systematics arise from the calibration of source galaxy shapes (Hernández-Martín et al. 2020), photometric redshift uncertainties in the background galaxy sample (Wright et al. 2020), contamination of the source sample by cluster member galaxies (Varga et al. 2019), and miscentering — offsets between the detected cluster centre and the true dark matter halo centre (Becker & Kravtsov 2011; Lee et al. 2018; Zhang et al. 2019; Sommer et al. 2022, Murray et al., in prep.). Additionally, selection effects from the cluster detection process can introduce correlations between lensing mass and observed richness that can significantly bias cluster abundance and lensing analyses (Wu et al. 2022; Zhang et al. 2024; Salcedo et al. 2024).

As the volume and precision of cosmological datasets improve, simplified likelihood assumptions tend to break down<sup>2</sup>, potentially compromising the robustness of inference. Working with next-generation survey data, which are not only high-volume but also high-precision, requires finer resolution in parameter space and more nuanced modeling of systematics. To address these limitations, the community is increasingly turning to Simulation-Based Inference (SBI), also known as Implicit-Likelihood Inference. From a methodological standpoint, SBI relies on (i) the generation of a synthetic dataset spanning a relevant range of cosmological and nuisance parameters, and (ii)

learning the probabilistic relationship between the simulated observables and the latent parameters. Simulation-based inference has already been successfully applied to real datasets, e.g. DES (Jeffrey et al. 2021; Gatti et al. 2025; Prat et al. 2026), KiDS (von Wietersheim-Kramsta et al. 2025), SDSS (Lemos et al. 2023b), and *Planck* cluster number counts (Zubeldia et al. 2025), showing good agreement with analytic likelihood-based approaches while naturally accounting for stochastic effects beyond the limitations of Gaussian likelihood assumptions. Several proof-of-concept studies, validated on mock datasets (Reza et al. 2022, 2024; Kosiba et al. 2025; Cerardi et al. 2025; Regamey et al. 2025; Sáez-Casares et al. 2026), have explored the potential of SBI from X-ray, SZ, and optical cluster samples, paving the way for the broader adoption of likelihood-free inference techniques in the analysis of current and upcoming cluster surveys.

In this paper, we present Capi.sh<sup>3</sup> (Cluster abundance posterior inference from simulated halos), a Python code dedicated to performing the cosmological analysis of optically-selected cluster catalogues in the era of the Vera C. Rubin LSST and the *Euclid* mission, using simulations. In Section 2, we present the different functionalities of the Capi.sh code. Its diagram is shown in Figure 1. We evaluate in Section 3 the internal calibration of Capi.sh simulations and self-applied cosmological analyses, as well as by using the *Euclid* Flagship dark matter halo catalogue. We conclude in Section 4.

## 2. The Capi.sh code

Capi.sh is dedicated to (i) simulate analytically galaxy cluster catalogues, given cosmological parameters, survey characteristics, and some observational systematics, (ii) training Neural Density Estimators (NDE), and (iii) performing the cosmological analyses of cluster catalogues from the trained NDE. The code structure of Capi.sh is presented in Figure 1.

<sup>2</sup> i.e., the underlying likelihood function is either unknown, unavailable, or computationally too expensive

<sup>3</sup> <https://github.com/calumhrmurray/capish>

## 2.1. Generating dark matter halo catalogues

Capish generates a dark matter halo catalogue from a halo mass function (e.g., Tinker et al. 2008, 2010; Despali et al. 2016). We first compute the halo count prediction  $N_{ij}$  in narrow mass bins (between  $\log_{10} m = 12$  to  $\log_{10} m = 16.5$ ) with width  $\Delta \log_{10} m_i \ll 1$  and redshift bins (between  $z = 0$  to  $z = 1.2$ ) with width  $\Delta z_j \ll 1$ , given as

$$N_{ij}^{\text{grid}} = \Delta \log_{10}(m_i) \Delta z_j n_h(\log_{10} m_i^{\text{center}}, z_j^{\text{center}}) \quad (1)$$

where  $\log_{10} m_i^{\text{center}}$  (resp.  $z_j^{\text{center}}$ ) is the center of the  $i$ -th log-mass (resp.  $j$ -th redshift) bin. In the above equation,  $n_h(m, z)$  is the predicted total halo number density per mass and redshift range given by

$$n_h(\log_{10} m, z) = \Omega_S \frac{dn(\log_{10} m, z)}{d \log_{10} m} \frac{d^2 V(z)}{dz d\Omega} \quad (2)$$

where  $dn(m, z)/dm$  is the halo mass function of objects at redshift  $z$  and mass  $m$ ,  $\Omega_S$  is the survey solid angle and  $V(z)$  the comoving volume.

The intrinsic clustering of the underlying matter density field induces a covariance in halo counts. This is often referred to as Super-Sample Covariance (SSC, Hu & Kravtsov 2003), and is an important contribution to the variance of large-scale structure probes (particularly galaxy clusters, Fumagalli et al. 2021; Payerne et al. 2023) as cosmological surveys increase in coverage and depth. SSC is usually accounted for in the binned count analytic likelihood as an additional covariance term. The effect of SSC is as a correlated scattering of the per-bin halo count prediction in Eq. (1), such as

$$\tilde{N}_{ij}^{\text{grid}} = N_{ij}^{\text{grid}} (1 + \delta_{ij}^{\text{SSC}}) \quad (3)$$

where  $\delta_{ij}^{\text{SSC}}$  is the scattering associated to the SSC, which satisfies  $\langle \delta_{ij}^{\text{SSC}} \rangle = 0$  and  $\langle \delta_{ij}^{\text{SSC}} \delta_{kl}^{\text{SSC}} \rangle = b_{ij} b_{kl} \sigma_{\text{SSC},jl}^2$ , where  $b_{ij}$  is the halo bias at mass  $m_i$  and redshift  $z_j$ , and (Lacasa et al. 2018, 2023)

$$\sigma_{\text{SSC},jl}^2 = \frac{4\pi}{\Omega_S} \int \frac{k^2 dk}{2\pi^2} j_0[kw(z_j)] j_0[kw(z_l)] P_{\text{mm}}(k|z_j, z_l) \quad (4)$$

is the (partial-sky) amplitude of matter density fluctuations<sup>4</sup>. In the equation above,  $j_0(x) = \sin(x)/x$  is the zero-th order spherical Bessel function, and  $P_{\text{mm}}(k|z_1, z_2)$  is the linear matter power spectrum. In the unbinned regime (given by  $\Delta z_j \ll 1$ , see e.g. Mantz et al. 2010; Penna-Lima et al. 2014), the variance of  $\delta_{ij}^{\text{SSC}}$  becomes maximal, such as the occurrence  $\delta_{ij}^{\text{SSC}} < -1$  becomes statistically significant if  $\delta_{ij}^{\text{SSC}}$  is considered to be a Gaussian variable. This could yield to un-physical halo counts through Eq. (3) (Payerne et al. 2024). In this regime, it is more appropriate to consider  $\delta_{ij}^{\text{SSC}}$  as a log-normal random variable (Coles & Jones 1991; Wen et al. 2020), such as  $\ln(1 + \delta^{\text{SSC}}) \sim \mathcal{N}(\mu^{\text{SSC}}, \Sigma^{\text{SSC}})$  where

$$\mu_{ij}^{\text{SSC}} = -\frac{1}{2} \ln(1 + b_{ij}^2 \sigma_{\text{SSC},jj}^2) \quad (5)$$

$$\Sigma_{ij,kl}^{\text{SSC}} = \ln(1 + b_{ij} b_{kl} \sigma_{\text{SSC},jl}^2) \quad (6)$$

<sup>4</sup> We use PySSC (Lacasa & Grain 2019; Gouyou Beauchamps et al. 2022) to compute  $\sigma_{\text{SSC},jl}$  (we use the PySSC function `sigma2_fullsky`, then rescaled by the sky fraction  $\Omega_S/4\pi$ ). The code is available at <https://github.com/fabienlacasa/PySSC>.

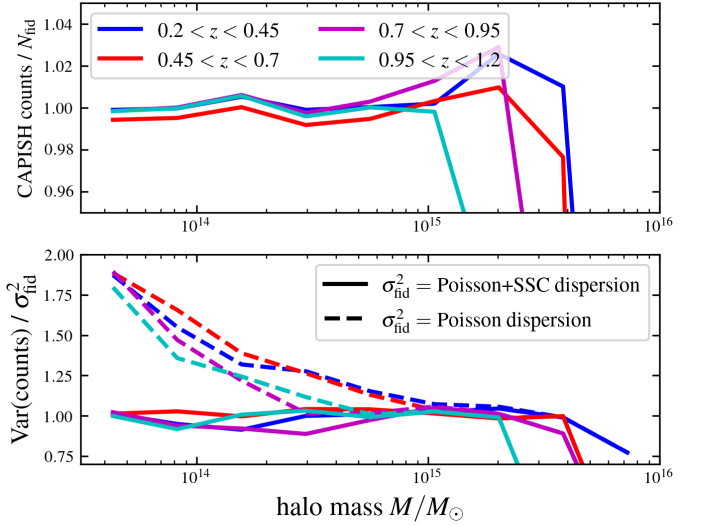


**Fig. 2.** Upper panel: Mean Capish halo count compared to analytical prediction. Lower panel: Variance of Capish halo counts compared to Poisson-only or Poisson+SSC variance analytical prediction.

such as the aforementioned conditions for  $\langle \delta_{ij}^{\text{SSC}} \rangle$  and  $\langle \delta_{ij}^{\text{SSC}} \delta_{kl}^{\text{SSC}} \rangle$  are satisfied. Finally, the number of halos is sampled from a Poisson distribution  $\mathcal{P}$  such as

$$\tilde{N}_{ij}^{\text{grid}} \sim \mathcal{P}[\tilde{N}_{ij}^{\text{grid}}]. \quad (7)$$

The resulting dark matter halo catalogue is obtained by collecting  $\tilde{N}_{ij}^{\text{grid}}$  times samples drawn randomly inside the mass-redshift bin, with center  $m_i$  and  $z_j$ . In the upper panel of Figure 2, we show the ratio between (i) the mean of 200 simulated dark matter halo counts with Capish in large mass-redshift bins (for display purposes, to compare with binned prediction) and (ii) the associated theoretical prediction  $N_{ij}^{\text{true}}$ , computed as the two-dimensional integral of the halo density in Eq. (2) within the same large mass-redshift bins. The ratio is close to 1 for most mass scales, except at high-mass, where the measured halo abundance is smaller than the cosmological prediction, because of the finite volume of the simulated catalogue. Additionally, we compute the dispersion of halo number counts in the same mass-redshift bins, which we compare to the theoretical variance given by<sup>5</sup> (Takada & Spergel 2014; Lacasa & Grain 2019)

$$\text{Var}(N_{ij}) = N_{ij}^{\text{true}} + (N_{ij}^{\text{true}})^2 \langle b_{ij} \rangle^2 S_{jj} \quad (8)$$

as the sum of a Poisson term and an SSC term, where  $\langle b_{ij} \rangle$  is the mean halo bias in the mass-redshift bin and  $S_{kl}$  is given by<sup>6</sup> (Lacasa et al. 2018)

$$S_{kl} = \int_{z_k}^{z_{k+1}} \int_{z_l}^{z_{l+1}} \frac{dV(z') dV(z'')}{V_k V_l} \sigma_{\text{SSC}}^2(z', z''), \quad (9)$$

where  $dV(z)$  is the comoving volume per steradian ( $V_k$  is the total volume in the  $k$ -th redshift bin). In the bottom panel of Figure 2, we see that the measured count dispersion has a good agreement with analytic count variance at most mass scales. We also see that SSC is important for lower mass halos; therefore, from this example, we show that our implementation of SSC in our simulation-based framework is in agreement with the behavior

<sup>5</sup> We use the Tinker et al. (2010) halo bias for the SSC part.

<sup>6</sup> We use the `Sij_fullsky` function of PySSC, then rescaled to the sky fraction  $\Omega_S/4\pi$ .

of SSC in the analytical likelihood analysis. The resulting dark matter halo catalogue serves as a basis to generate the catalogue of observed galaxy clusters.

## 2.2. Generating galaxy cluster catalogue

### 2.2.1. From halo properties to cluster observables

The dark matter halo catalogues has to be connected to observational cluster properties, such as the observed richness and the weak gravitational lensing signal. We use a general multi-variate Gaussian model (Evrard et al. 2014; Zhang et al. 2024; Payerne et al. 2025) for the observed richness  $\lambda_{\text{obs}}$  and a lensing observable, corresponding to the lensing mass  $\log_{10} m_{\text{WL}}$ , i.e.

$$\ln \lambda_{\text{obs}}, \log_{10} m_{\text{WL}} \sim \mathcal{N}[\text{mean}(m, z), \text{Cov}(m, z)] \quad (10)$$

where

$$\text{mean}(m, z) = \{\langle \ln \lambda_{\text{obs}} | m, z \rangle, \langle \log_{10} m_{\text{WL}} | m, z \rangle\} \quad (11)$$

and

$$\text{Cov}(m, z) = \begin{pmatrix} \sigma_{\ln \lambda}^2 & \rho \sigma_{\ln \lambda} \sigma_{\text{WL}} \\ \rho \sigma_{\ln \lambda} \sigma_{\text{WL}} & \sigma_{\text{WL}}^2 \end{pmatrix}. \quad (12)$$

We define the cluster richness  $\lambda_{\text{obs}}$  as related to the count of cluster's member galaxies – intrinsically linked to the cluster's formation history – evaluated, e.g., within a circular aperture centered on the detected cluster position (à-la redMaPPer, Rykoff et al. 2014). The observed richness is linked to the specific selection of these galaxies in photometric surveys, therefore it depends on the cluster detection algorithm to define and measure the cluster's richness<sup>7</sup> (Rykoff et al. 2014; Bellagamba et al. 2018; Aguena et al. 2021) (ii) observational/detection noise. A power-law relation (see e.g. Mantz et al. 2008; Evrard et al. 2014; Saro et al. 2015; Farahi et al. 2018; Murata et al. 2019; Anbajagane et al. 2020) is commonly adopted to connect the mean cluster's observed (log-) richness  $\ln \lambda_{\text{obs}}$  with its halo mass and redshift, via

$$\langle \ln \lambda_{\text{obs}} | m, z \rangle = \mu_0^\lambda + \mu_m^\lambda \log_{10} \left( \frac{m}{m_0} \right) + \mu_z^\lambda \log \left( \frac{1+z}{1+z_0} \right). \quad (13)$$

Two contributions affect the measurement scatter of the cluster's richness. First, the intrinsic scatter ( $\sigma_{\ln \lambda, \text{int}}$ ) denotes for the contribution of the intrinsic cluster's formation history. Second, Poisson sampling arises as a statistical process on its own, associated with the observation, since richness is a "count-in-cell" observable. In this work, we use (Farahi et al. 2018; Zhang et al. 2023; To et al. 2025)

$$\sigma_{\ln \lambda}^2 = \sigma_{\ln \lambda, \text{int}}^2 + \exp\{-\langle \ln \lambda_{\text{obs}} | m, z \rangle\}. \quad (14)$$

where the first term denotes the intrinsic scatter and the second the Poisson dispersion<sup>8</sup> of the richness measurement. This is currently the primary weakness of Capish, as the actual relation

<sup>7</sup> Generally scaling with, but not equal to, the number counts of member galaxies inside clusters. For instance, Rykoff et al. (2014) defines the richness as the sum of membership probabilities for red-sequence-selected galaxies in the vicinity of a cluster, where Aguena et al. (2021) define clusters as the overlap of multiple galaxy's photometric redshift distributions happening at the same position on the sky.

<sup>8</sup> Most papers uses  $(\exp(\langle \ln \lambda_{\text{obs}} | m, z \rangle) - 1) / \exp(2\langle \ln \lambda_{\text{obs}} | m, z \rangle)$ , which is a good approximation for large richness values. Since we want our code to be stable over the full richness range, we use Eq. (14).

between halo mass and observed cluster richness is likely much more complex.

Galaxy cluster lensing masses are primarily inferred from the weak gravitational lensing effects of the cluster's gravitational potential, inducing a small distortion in the shapes of background galaxies. This is generally estimated from the excess surface density (Murray et al. 2022), which is taken to be the average in projected radial bins around the cluster center of the weighted background ellipticities  $\widehat{\Delta\Sigma}(R) = \langle \Sigma_{\text{crit}}(z_s, z_l) \epsilon_+^{l,s} \rangle(R)$  where  $\Sigma_{\text{crit}}(z_s, z_l)$  is the critical surface mass density – a geometrical lensing factor – and  $\epsilon_+^s$  is the tangential ellipticity of a source at  $z_s > z_{\text{cl}}$  within the radial bin. The excess surface density in radial bins is not the unique cluster weak lensing signal estimator that is used in the literature; one can also use the binned reduced shear (Becker & Kravtsov 2011), two-dimensional lensing maps (Oguri et al. 2010, Murray et al., in prep.), or weak lensing shear magnification (Murray et al. 2025). The measured excess surface density profile probes  $\Sigma(R|m)$ , to be the projected three-dimensional matter density  $\rho_{\text{cl}}(\mathbf{x})$  in the cluster field. The cluster lensing mass  $m_{\text{WL}}$  (along with other halo parameters such as its concentration) is obtained by fitting the lensing profile with the appropriate model for the matter density around cluster center<sup>9</sup> (McClintock et al. 2019). The lensing mass  $m \rightarrow m_{\text{WL}}$  could be biased with respect to its true underlying halo mass, so we use the power-law relation

$$\langle \log_{10} m_{\text{WL}} | m, z \rangle = \mu_0^{\text{WL}} + \mu_m^{\text{WL}} \log_{10} m + \mu_z^{\text{WL}} \ln \left( \frac{1+z}{1+z_0} \right). \quad (15)$$

In the above equation, any deviation from  $\mu_0^{\text{WL}} = 0, \mu_m^{\text{WL}} = 1$  and  $\mu_z^{\text{WL}} = 0$  indicates that the lensing masses are biased with respect to the true halo mass, which may happen if the underlying dark matter density profile is not accurately representing lensing data.

The lensing profile  $\widehat{\Delta\Sigma}(R)$  is a scattered measurement, arising for several independent contributions (Hoekstra 2001, 2003; Becker & Kravtsov 2011; Gruen et al. 2015; Wu et al. 2019). Its dominant noise term ( $\sigma_{\text{WLgal}}^{\Delta\Sigma}$ ) arises from intrinsic galaxy shape dispersion and limited source galaxy samples for the lensing profile estimation, scaling as  $\sigma_\epsilon / \sqrt{\bar{n}_{\text{gal}}(z)}$ , where  $\sigma_\epsilon^2 = \sigma_{\epsilon, \text{meas.}}^2 + \sigma_{\epsilon, \text{SN}}^2$  being the dispersion of galaxy shapes due to (i) intrinsic galaxy shape noise ( $\sigma_{\epsilon, \text{SN}} \approx 0.25$ , Chang et al. 2013), (ii) errors in shape measurement algorithms ( $\sigma_{\epsilon, \text{meas.}}$ ), and  $\bar{n}_{\text{gal}}(z)$  the surface number density of lensed background galaxies for a cluster at redshift  $z$ . Additional noise— independent of source density—comes from the intrinsic dispersion in halo morphology<sup>10</sup> ( $\sigma_{\text{WLint}}^{\Delta\Sigma}$ ) and the impact of correlated/uncorrelated large-scale structure ( $\sigma_{\text{WLCSS}}^{\Delta\Sigma}$  and  $\sigma_{\text{WLuLSS}}^{\Delta\Sigma}$ ). On the observational side, further systematics arise from shape measurement errors (Hernández-Martín et al. 2020), photometric-redshift uncertainties (Wright et al. 2020), cluster-member contamination (Varga et al. 2019), and miscentering (Zhang et al. 2019; Sommer et al. 2022). As a summary, the total variance  $\sigma_{\text{WL}}^{\Delta\Sigma}$  of the measured excess surface density profile  $\Delta\Sigma(R)$  is given by the quadratic sum of these terms. The lensing profile variance depends on the underlying halo mass, its redshift, but also its local environment, and finally the lensing survey characteristics. In this work, we

<sup>9</sup> We generally consider that the lensing signal is dominated by the 1-halo term at scales below 3 Mpc, originating from the cluster itself, and the 2-halo term become increasingly important at larger scales, originating by neighboring halos.

<sup>10</sup> Because most of the time we use a simplified spherical model to constrain the mass of non-spherical clusters.

rely on the lensing mass; its variance – as for the lensing profile – can be decomposed as

$$\sigma_{\text{WL}}^2 = \sigma_{\text{WLgal}}^2 + \sigma_{\text{WLint}}^2 + \sigma_{\text{WLcLSS}}^2 + \sigma_{\text{WLuLSS}}^2. \quad (16)$$

The above depends on the number of parameters (and correlations) that are fitted jointly with the lensing mass (see Appendix A). For simplicity in this work, we will only consider the  $\sigma_{\text{WLgal}}^2$  component, and leave the implementation of the other terms for future works, which can be obtained separately from theory (Shirasaki & Takada 2018) of dedicated simulations (Becker & Kravtsov 2011; Wu et al. 2019, Murray et al. in prep.). As the number density of sources approaches that expected from space-based observations or LSST conditions (e.g. DES provided  $\bar{n}_{\text{gal}} = 10 \text{ arcmin}^{-2}$ , where LSST will provide  $\bar{n}_{\text{gal}} = 40 \text{ arcmin}^{-2}$ ), the contribution to the scatter in the weak lensing masses from galaxy shape noise becomes comparable or even subdominant to the intrinsic scatter terms and large-scale structures (Hoekstra 2001; Becker & Kravtsov 2011). A fixed parameter can be used, but Capish also provides an information matrix-based analytical model  $\sigma_{\text{WLgal}}(m, z)$  as explained in Appendix A, for improved realism, as shown in Figure A.1, accounting for (i) the cluster’s redshift-dependent number density of source galaxies, (ii) the theoretical modeling for  $\Delta\Sigma(R)$  and (iii) the considered radial fitting range. In this error model, the scatter is larger for low-mass halos (whose weak lensing signals have a lower signal-to-noise ratio), or high-redshift halos (which have fewer source galaxies to measure their lensing profiles).

Within Capish, it is also possible instead to add lensing mass scatter at the *summary statistics level* accordingly with  $\sigma_{\text{WL}}^{\text{stack}} = \sigma_{\text{WL}} / \sqrt{N}$ , where  $N$  is the total number of clusters in the stack. This is closer to the modelling used in recent cluster cosmology analyses and weak lensing mass-relation calibration technique (Abbott et al. 2020; Lesci et al. 2025; Payerne et al. 2025), where the *mean* mass of clusters is inferred from a stack of cluster weak lensing profiles. This is discussed in Section 2.3, when addressing how lensing mass summary statistics are built. In this case, there is no difference in considering  $\log_{10} m_{\text{WL}}$  or  $m_{\text{WL}}$  as the random Gaussian lensing variable.

For optically-selected clusters, an important systematic is the covariance between the lensing observable and the observed richness that is assigned by cluster finders. This covariance induces additive biases that cannot be mitigated by increasing source density or reducing shape noise (Nord et al. 2008; Evrard et al. 2014; Farahi et al. 2018; Wu et al. 2019; Nyarko Nde et al. 2025), yet must be accurately quantified to achieve percent-level mass calibration (Rozo et al. 2014; Zhou et al. 2024). The intrinsic part of this covariance reflects galaxy assembly bias tied to secondary halo properties such as concentration, mass accretion rate, or dynamical state (Zhang et al. 2024). The extrinsic part arises from selection biases within cluster-finding algorithms (Wu et al. 2019), shaped by observational systematics, including photometric-redshift errors (Graham et al. 2018), shear shape noise (Wu et al. 2019), projection and percolation effects (Costanzi et al. 2019), triaxiality bias (Zhang et al. 2023), and additional complexities associated with realistic cluster finders such as redMaPPer (Rykoff et al. 2014). We define  $\rho = \text{Corr}(\log_{10} m_{\text{WL}}, \ln \lambda_{\text{obs}} | m, z)$  to be the overall correlation coefficient between the lensing observable and observed richness at fixed true mass and redshift. This correlation coefficient is effective, with no distinction between intrinsic and extrinsic scatters (Wu et al. 2019; Zhou et al. 2024).

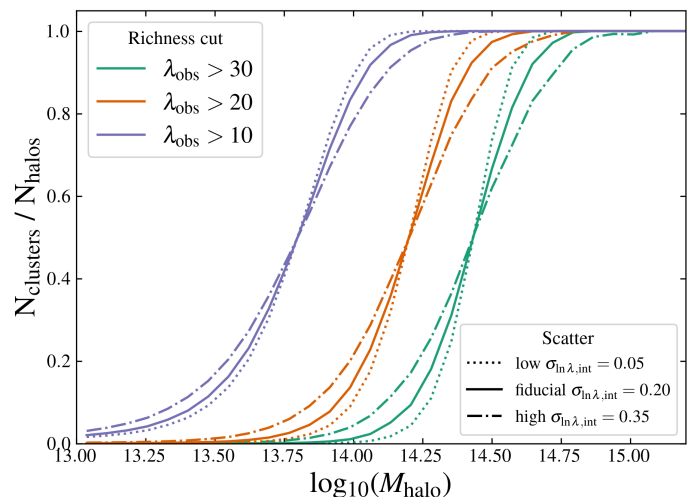


**Fig. 3.** Completeness of the simulated cluster catalogue as a function of halo mass for different observed richness thresholds, and intrinsic richness–mass scatter  $\sigma_{\ln\lambda, \text{int}}$  in Eq. (14). Lower richness thresholds and smaller intrinsic richness–mass scatter yield higher completeness at fixed mass, with all curves asymptoting to unity at high mass.

### 2.2.2. Cluster photometric redshifts

Individual observed cluster’s redshift are usually derived from their member galaxies (see e.g. Rykoff et al. 2014). It is linked to the redshift of its underlying dark matter halo through

$$z_{\text{phot}} \sim \mathcal{N}(z + b(z), \sigma_{\text{PZ}}(z)^2), \quad (17)$$

where  $b(z)$  represents a possible systematic bias, and  $\mathcal{N}(0, \sigma_{\text{PZ}}^2)$  denotes a Gaussian random variable with zero mean and redshift-dependent scatter  $\sigma_{\text{PZ}}(z) = \sigma_{\text{PZ},0}(1 + z)$ , and depends on the optical survey characteristics, depth, etc, setting  $\sigma_{\text{PZ},0}$  at  $z = 0$ . This functional form captures the typical uncertainty increase at higher redshifts due to observational limitations.

### 2.2.3. Cluster selection function

A key advantage of simulation-based inference is that the selection function should emerge naturally from the forward model rather than being imposed externally. In Capish, the probability of detecting a cluster at a given halo mass (the survey completeness) is determined by whether its observed richness exceeds the survey threshold. This means the selection function is encoded in the mass-observable relation: a cluster is selected when its scattered richness lands above the detection limit.

The Figure 3 illustrates this for mass-observable relation parameters matched to DES-Y1 (see Table 1), showing how completeness varies with halo mass for different richness thresholds and intrinsic scatter values. Lower thresholds and smaller scatter both steepen the selection function and push it to lower masses. A more realistic mass-richness relation, for example, that from Salcedo et al. (2024), would lead to many more low mass clusters being included within the sample. This approach requires a mass-richness relation of sufficient fidelity to capture the true selection. The ideal framework would forward model the full pipeline: galaxy catalogue, cluster detection algorithm, and richness assignment. This is beyond our current scope. An alternative approach to implementing completeness independently of the mass–richness relation is presented in Appendix B, following the formalism of, e.g., Rozo et al. (2010); Aguena & Lima

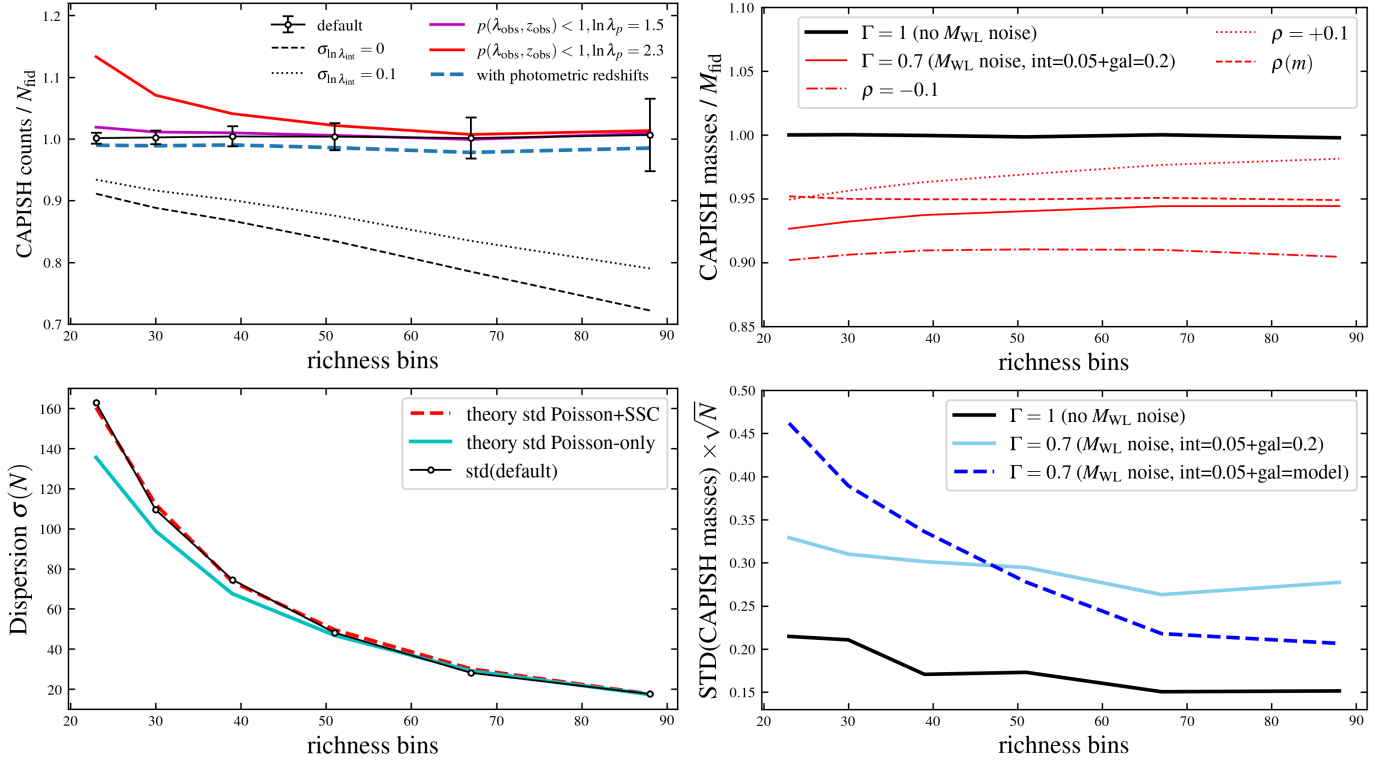


**Fig. 4.** Left: Upper panel: CapiSh mean mass outputs, averaged over 100 simulations, compared to the theoretical prediction for the mean mass of a stack of clusters in redshift richness bins. Lower panel: Standard deviation of the same mean masses over the 100 simulations. Right: Upper panel: CapiSh mean count outputs, averaged over 100 simulations, compared to the theoretical prediction for the mean cluster count of a stack of clusters in redshift richness bins. Lower panel: Standard deviation of the same counts over the 100 simulations.

(2018); Lesci et al. (2022); Lesci et al. (2025); Payerne et al. (2025).

Additionally, optical surveys suffer from artifacts—unmasked stellar diffraction spikes, globular clusters misidentified as galaxy overdensities, line-of-sight projections—that inject spurious detections into the catalogue. We therefore include a purity model in CapiSh to account for these false positives. We define the purity  $p(\lambda_{\text{obs}}, z_{\text{phot}})$  as the fraction of detected objects that correspond to genuine clusters. Following Aguena & Lima (2018), we adopt the form

$$p(\lambda_{\text{obs}}, z_{\text{obs}}) = \frac{(\lambda_{\text{obs}}/\lambda_p)^{n_{\text{pur}}(z_{\text{obs}})}}{1 + (\lambda_{\text{obs}}/\lambda_p)^{n_{\text{pur}}(z_{\text{obs}})}}, \quad (18)$$

where  $n_{\text{pur}}$  and  $\lambda_p$  set the shape and scale of the purity function. This parameterization ensures purity approaches unity at high richness while allowing significant contamination at low richness, consistent with the behavior of real cluster finders. For each richness-redshift bin, we first compute the histogram of true detections  $\hat{N}_{\text{true}}(\lambda_{k,\text{obs}}, z_{l,\text{phot}})$ , then draw the number of spurious detections from:

$$\hat{N}_{kl,\text{fake}} \sim \mathcal{P}\left(\hat{N}_{\text{true}}(\lambda_{k,\text{obs}}, z_{l,\text{phot}}) \times \frac{1 - p(\lambda_{k,\text{obs}}, z_{l,\text{phot}})}{p(\lambda_{k,\text{obs}}, z_{l,\text{phot}})}\right). \quad (19)$$

Each spurious detection is assigned a richness and redshift drawn uniformly within its bin. We set the lensing mass of these objects to zero, reflecting the assumption that they produce a negligible weak lensing signal<sup>11</sup>.

<sup>11</sup> Any identified structure would inevitably produce a positive lensing signal, as it may consist of a low-mass population or result from the

### 2.3. Cluster count and cluster lensing summary statistics

CapiSh returns two summary statistics;

- **Count in richness-redshift bins:** The cluster abundance summary statistic is the measured counts in bins of observed richness and photometric redshifts, such as

$$\widehat{N}_{kl} = \sum_{\text{cl}} \delta_{\text{cl} \in (k,l)}^K. \quad (20)$$

- **Mean mass in richness-redshift bins:** The mean mass in a given richness-redshift bin is given as the mean of individual lensing masses. However, the usual way to recover the mean lensing mass of clusters within the  $kl$ -th observed richness-observed redshift bins is to fit the corresponding stacked lensing profile  $\widehat{\Delta \Sigma}_{kl}$  in the same  $kl$  richness-redshift bin (see e.g. Murata et al. 2019). From this, the link between the "true" mean mass of a stack and the mean mass inferred from the weak lensing stacked profile  $\widehat{\Delta \Sigma}_{kl}$  may not be trivial and may be affected by the dispersion of individual masses within the stack (McClintock et al. 2019). Melchior et al. (2017) proposed that since  $\Delta \Sigma(R|M) \propto M^{\Gamma(R|M)}$  (at first order) where  $\Gamma(R|M)$  is the logarithmic slope of the excess surface density<sup>12</sup>, we use  $\Gamma = 0.7$  in this work; the mean weak lensing mass inferred from  $\widehat{\Delta \Sigma}_{kl}$  (Abbott et al.

cumulative contribution of projected structures along the line of sight; however, this has not been explored extensively in the literature, and this is not the purpose of this work, so we keep using the aforementioned assumption.

<sup>12</sup> For instance, Melchior et al. (2017) found a typical value of  $\Gamma = 0.74$  for an NFW profile within the one-halo regime.

2020; Lesci et al. 2022; Fumagalli et al. 2023) can be modeled/interpreted as

$$\widehat{M}_{kl} = \left( \frac{1}{\sum_{cl} W(z_{cl}) \delta_{cl \in (k,l)}^K} \sum_{cl} W(z_{cl}) m_{cl,WL}^\Gamma \delta_{cl \in (k,l)}^K} \right)^{1/\Gamma} \quad (21)$$

where, considering  $\sigma_\epsilon^2(z_s) = \sigma_{\epsilon,\text{meas.}}^2(z_s) + \sigma_{\epsilon,\text{SN}}^2(z_s)$  (in this work, we set  $\sigma_{\epsilon,\text{meas.}} = 0$ ), the weights  $W(z_{cl})$  are the maximum signal-to-noise ratio weights (Sheldon et al. 2004) and are given by

$$W(z_{cl}) = \frac{1}{\int_{z_{cl}}^\infty dz'_s n_{\text{gal}}(z'_s)} \int_{z_{cl}}^\infty dz'_s n_{\text{gal}}(z'_s) \frac{\Sigma_{\text{crit}}^{-2}(z'_s, z_{cl})}{\sigma_\epsilon^2(z'_s)}, \quad (22)$$

where  $n_{\text{gal}}(z)$  is the source galaxy redshift distribution, taken from Chang et al. (2013).

As stated in Section 2.2, a choice is to consider that (i) individual masses are not scattered in Eq. (12), and (ii) that the weak lensing mass scatter is instead applied at the *stacked* level, such as

$$\log_{10} \widehat{M}_{kl} \rightarrow \log_{10} \widehat{M}_{kl} + \widehat{\epsilon}_{kl}, \quad (23)$$

where  $\widehat{\epsilon}_{kl} \sim \mathcal{N}(0, (\sigma_{\text{WL},kl}^{\text{stack}})^2)$ . The stacked scatter is given

by  $\sigma_{\text{WL},kl}^{\text{stack}} = \sigma_{\text{WL},kl} / \sqrt{N_{kl}}$ , with  $\sigma_{\text{WL},kl}$  denoting the weak lensing mass scatter for a single cluster lying in the  $(k, l)$  richness-redshift bin. This quantity  $\sigma_{\text{WL},kl}$  is either fixed or evaluated using the error model for the mean mass of the stack (see Appendix A). This is useful if we want to match the lensing mass error bars that are obtained in a given analysis by just setting them manually.

The simulated cluster count may become zero in one or more richness-redshift bins for a given simulation. In that case, it is not possible to compute the appropriate mean cluster mass for the corresponding bins. As an output of Capish and as input of the neural density estimators (see the next section), we use the "mass" summary statistics

$$\widehat{NM}_{kl} = \begin{cases} \widehat{N}_{kl} \times \widehat{M}_{kl} & \text{if } \widehat{N}_{kl} \neq 0 \\ 0 & \text{if } \widehat{N}_{kl} = 0 \end{cases} \quad (24)$$

where  $\widehat{N}_{kl}$  is given in Eq. (20), and  $\widehat{M}_{kl}$  is given in Eq. (21). So, Eq. (24) is set to 0 when the bin is unfilled, instead of being not defined. This enables us to smooth the summary statistics for extreme cases, which will facilitate the training of neural density estimators.

### 3. Validation

#### 3.1. Validating Capish outputs

Before any cosmological analysis, we can explore how Capish outputs compare to the theoretical prediction of cluster counts and cluster masses (see Appendix E). For the redshift bin  $0.2 < z < 0.5$  and in 7 richness bins, we show in Figure 4 (left panel, upper plot) the bias between the mean Capish-counts (averaged over 100 simulations) and a analytical count prediction in Eq. (E.1), that is computed without accounting for selection function with fiducial parameters listed in Table 1 (the underlying halo mass definition used through this work is  $M_{200m}$ , and we used the Tinker et al. (2010) halo mass function). For the

Parameters	Default values in Capish	Equations
$(\Omega_m, \Omega_b)$	(0.319, 0.048)	Eq. (2)(4)
$(\sigma_8, n_s)$	(0.813, 0.96)	-
$h$	0.7	-
$(w_0, w_a)$	(-1, 0)	-
$\Omega_S$	$\pi/2$ ( $f_{\text{sky}} = 1/8$ )	-
$(\mu_0^\lambda, \mu_m^\lambda, \mu_z^\lambda)$	(3.5, 1.72, 0.0)	Eq. (13)
$(\log_{10} m_0, z_0)$	(14.5, 0.5)	-
$\sigma_{\ln \lambda, \text{int}}$	0.2	Eq. (14)
$\rho$	0	Eq. (12)
$(\mu_0^{\text{WL}}, \mu_m^{\text{WL}}, \mu_z^{\text{WL}})$	(0, 1, 0)	Eq. (15)
$(\sigma_{\text{WLgal}}, \sigma_{\text{WLint}})$	(0.2 or theory-based, 0)	Eq. (16)
$(\sigma_{\text{PZ},0}, b(z_{\text{true}}))$	(0, 0)	Eq. (17)
$(n_{\text{pur}}, \ln \lambda_p)$	(2.5, 1.5)	Eq. (18)
$(\alpha_{\text{gal}}, \beta_{\text{gal}}, z_{\text{gal}}^0)$	(2.0, 1.5, 0.5)	Eq. (A.4)
$\Gamma$	0.7	Eq. (21)

**Table 1.** Fiducial values for Capish. The halo mass function is taken from Despali et al. (2016) and the halo bias from Tinker et al. (2010). The first block corresponds to the fiducial cosmological parameters. The second block is for generating the cluster catalogue from the underlying halo catalogue. The last block is for computing summary statistics from the cluster catalogue. The parameters  $\mu_0^\lambda$ ,  $\mu_m^\lambda$  and  $\mu_z^\lambda$  are chosen to mimic the DES Y1 best fit of the cluster mass-richness relation (Abbott et al. 2020), the latter following a different parametrization.

simplest case (no selection function), Capish counts are in good agreement with the theoretical prediction. Accounting for the selection function<sup>13</sup>, we see that adding purity to Capish simulations affects the recovered counts at low richness, by adding fake clusters. We also see that adding photometric redshift induces a 2-3% bias with respect to the true redshift case. Figure 4 (left panel, lower plot), we see that the variance of Capish counts is in good agreement with the analytical prediction of cluster count variance, accounting for Poisson noise and SSC in Eq. (E.3).

Figure 4 (right panel, upper plot) the bias between the mean simulated Capish masses and a mean-mass prediction (computed using Eq. (E.5)), again with the simplest assumptions (i) no selection function (ii) no scatter for the lensing mass and (i)  $\Gamma = 1$ . When Capish is run under these simplest assumptions, the bias is zero. Introducing a slope  $\Gamma = 0.7$  produces a 5% bias, and adding noise – from galaxy shape/shot noise and intrinsic scatter (0.2 and 0.05, respectively) – to the lensing mass (assuming the  $\log_{10} m_{\text{WL}}$  parametrization) increases this bias to 10%. Furthermore, varying the constant correlation parameter  $\rho \in \{-0.1, +0.1\}$  causes the mean lensing masses to be biased low and high, respectively. More realistically, Capish allows the use of a mass-dependent function  $\rho(m) = 0.3 \times \exp(-2(\log_{10} m - 13.3))$ , decreasing with mass, whose effect on mean mass is more pronounced at lower richness (or lower mass) values. This is more realistic regarding the mass-dependence of selection bias (Sunayama et al. 2020; Wu et al. 2022; Zhou et al. 2024).

The right panel of Figure 4 (lower plot) shows the dispersion of the Capish mean masses. In the absence of lensing-mass noise, the dispersion is at its lowest level, originating from Poisson and SSC sampling of the halo mass function. When lensing-mass noise is included, the dispersion increases accordingly. We also see that using the error model described in Appendix A

<sup>13</sup> The fiducial selection function parameters in Table 1 are chosen such that the cluster catalogue is increasingly purer at high richness, with 50% purity at a richness  $\lambda = 5$ .

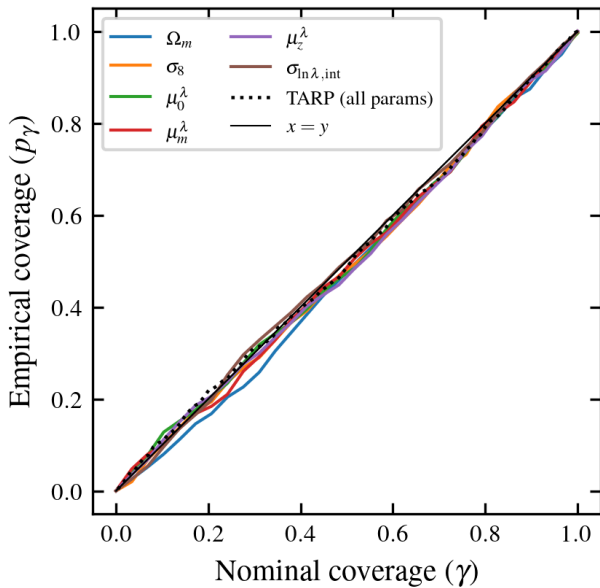


**Fig. 5.** Probability coverage tests using the estimated posterior over 6 Capish parameters, given the observation of counts and masses (count\_Nm). To prevent inaccuracies in the density estimation near prior boundaries, the neural posterior is trained on a broad prior, then restricted to a tighter one. The ECP calibration is computed for each parameter, and the TARP calibration is computed for all parameters at once.

(with  $\bar{n}_{\text{gal}} = 25 \text{ arcmin}^{-2}$ , and considering the fitting radius between 1 Mpc and 5 Mpc) increases the errors at low richness and decreases them at high richness, compared to adopting a fixed value for  $\sigma_{\text{WL}}$ . All of these preliminary tests of the Capish simulator ensure that the summary statistics behave as expected, as for their estimators and their covariances.

### 3.2. Probability coverage

The posterior prediction is built on top of the `sbi`<sup>14</sup> Python package (Tejero-Cantero et al. 2020), a flexible toolkit for SBI, whose inputs are summary statistic outputs obtained from the Capish simulator, and trains neural networks—typically normalizing flows—to learn the posterior  $\mathbb{P}(\hat{\theta}_{\text{true},k} | \hat{D}_k)$  using  $N_{\text{sim}}$  simulated pairs  $\{\hat{\theta}_{\text{true},k}, \hat{D}_k\}$  for  $k = 1, 2, \dots, N_{\text{sim}}$ , where  $\hat{D}_k \sim \text{Simulator}(\hat{\theta}_{\text{true},k})$ .

We assess the performance of the posterior generator across the free parameter space  $\theta = \{\Omega_m, \sigma_8, \mu_0^\lambda, \mu_m^\lambda, \mu_z^\lambda, \sigma_{\ln \lambda, \text{int}}\}$ . For the Capish simulator, we consider (i) a sky area of  $\Omega_S = \pi/2$  ( $f_{\text{sky}} = 1/8$ ), (ii) the Tinker et al. (2010) halo mass function with the 200m mass definition, (iii) pure cluster samples, (iv) the scaling functional form of the scaling relation in Eq. (13), (v) no photometric redshifts and (vi) we consider the stacked approach for the scatter of weak lensing mass, as explained in Section 2.3, and applied to the lensing mass through Eq. (23) with a theory model for  $\sigma_{\text{WL}}$  (with  $\bar{n}_{\text{gal}} = 25 \text{ arcmin}^{-2}$ , see Appendix A), (vii) using the alternative mass summary statistics in Eq. (24). Summary statistics (counts and modified lensing masses) are computed using richness bin edges  $\lambda = \{20, 30, 40, 60, 100, 200\}$  and redshift bin edges  $z = \{0.2, 0.35, 0.5, 0.7, 1.0\}$ , and whose input parameters. We generate  $N_{\text{sim}} = 60,000$  simulations covering the parameter priors  $\Omega_m \sim \mathcal{U}(0.2, 0.45)$ ,  $\sigma_8 \sim \mathcal{U}(0.6, 0.95)$ ,  $\mu_0^\lambda \sim \mathcal{U}(3, 4)$ ,

$\mu_m^\lambda \sim \mathcal{U}(1.3, 2.1)$ ,  $\mu_z^\lambda \sim \mathcal{U}(-0.7, 0.7)$ , and  $\sigma_{\ln \lambda, \text{int}} \sim \mathcal{U}(0.1, 0.5)$ , which encompass the fiducial values listed in Table 1.

We train the posterior generator using the Neural Posterior Estimator (NPE) method, using alternatively cluster counts in the dedicated richness-redshift bins (this configuration is labeled as count, see Eq. (20)), mean lensing masses multiplied by the cluster counts (labeled as Nm, see Eq. (24)), and the combination of the two (labeled as count\_Nm). After training, the `sbi` package returns a prediction for the posterior distribution for the six parameters  $\theta = \{\Omega_m, \sigma_8, \mu_0^\lambda, \mu_m^\lambda, \mu_z^\lambda, \sigma_{\ln \lambda, \text{int}}\}$ , given an observed data vector  $\hat{D}$  (being either cluster counts, cluster masses, or the combination of the two).

Validating the accuracy of the posterior generator is critical. To this end, we assess its performance using *coverage calibration test*, a key diagnostic of the posterior that tests if the reported posterior credible sets have their intended probabilistic meaning.

Given a dataset  $\hat{D}$  simulated at a parameter point  $\hat{\theta}_{\text{true}}$  drawn from the prior (i) we compute the corresponding posterior estimate  $\mathbb{P}(\hat{\theta} | \hat{D})$  from the trained NPE (ii) we extract a  $\gamma$ -credible set<sup>15</sup>  $\text{Cred}_\gamma(\hat{D})$  for this estimated posterior. For a nominal coverage probability  $\gamma$ , the Bayesian coverage expresses as,

$$p_\gamma(\hat{D}) := \mathbb{P}(\hat{\theta}_{\text{true}} \in \text{Cred}_\gamma(\hat{D}) | \hat{D}) \quad (25)$$

$$= \mathbb{E}_{\hat{\theta}_{\text{true}}} [\mathbb{1}\{\hat{\theta}_{\text{true}} \in \text{Cred}_\gamma(\hat{D})\} | \hat{D}]. \quad (26)$$

A posterior estimate is calibrated in the Bayesian sense if  $p_\gamma(\hat{D}) = \gamma$  for any  $\hat{D}$ , that is, the true parameter value  $\hat{\theta}_{\text{true}}$  should fall within the estimated posterior  $\gamma$ -credible set a fraction  $\gamma$  of the time, and so for any observed data  $\hat{D}$ . Under mild assumptions, this calibration is equivalent to the estimated posterior being equal to the true posterior. However, we don't have access to the true posterior by construction, and so the computation of  $p_\gamma$  from simulated pairs would require some binning of the observations. The common method is to average  $p_\gamma(\hat{D})$  also on data, i.e. over the simulated pairs  $\{\hat{\theta}_{\text{true},k}, \hat{D}_k\}$ , giving

$$p_\gamma := \mathbb{P}(\hat{\theta}_{\text{true}} \in \text{Cred}_\gamma(\hat{D})) = \mathbb{E}_{\hat{\theta}_{\text{true}}, \hat{D}} [\mathbb{1}\{\hat{\theta}_{\text{true}} \in \text{Cred}_\gamma(\hat{D})\}], \quad (27)$$

called Expected Coverage Probability (ECP). We say the posterior is calibrated with respect to ECP when  $p_\gamma = \gamma$ . We focus on the computation of ECP for the marginalized posteriors of the six considered parameters, and we plot their  $p_\gamma$  with respect to  $\gamma$ , such as in Figure 5. For information, a sub-identity  $p_\gamma < \gamma$  (resp. super-identity  $p_\gamma > \gamma$ ) calibration curve reveals an underestimation (resp. over-estimation) of the uncertainty.

This calibration test allows to detect some potential failures in the posterior estimation. For example, due to the continuous nature of the normalizing flows employed in the Neural Density Estimation (NDE), the posterior estimate can be heavily inaccurate nearby sharp posterior features such as prior edges (for example: Reza et al. (2024)). This leads to an underestimation of the probability density on the near the prior boundaries, such that a probability coverage test would exhibit a mild tendency toward overconfidence. First, we do not account for this effect and compute the ECP over the full prior range, for the three configurations (counts, mean masses, and their combination), as shown in Figure D.1, where it appears that  $p_\gamma < \gamma$ , i.e., the uncertainties are indeed under-estimated. We therefore recompute the same probability coverage for the count\_Nm configuration (combination of counts and mean masses, the most

<sup>15</sup> A  $\gamma$ -credible set is a set that contains the parameter value with probability  $\gamma$ , e.g. the interval between the  $\gamma/2$ -quantile and the  $1 - \gamma/2$ -quantile in 1D.

<sup>14</sup> <https://sbi-dev.github.io/sbi/latest/>

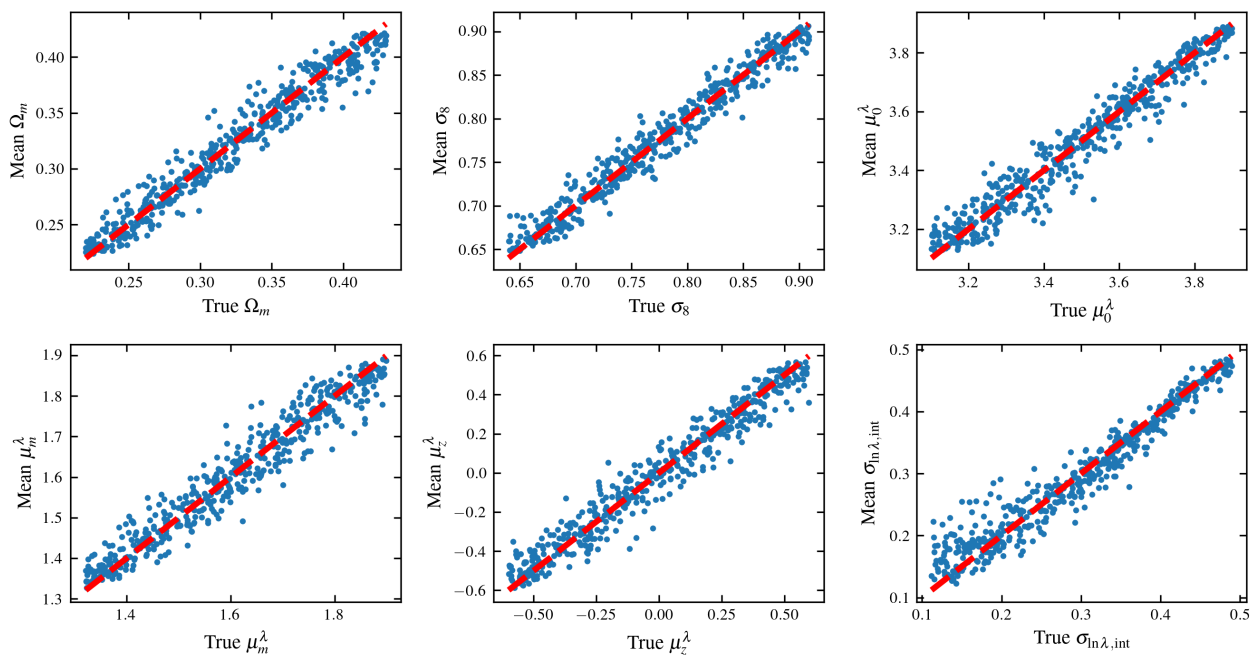


**Fig. 6.** Recovered mean parameters versus true input values for the `count_Nm` configuration, computed from 500 simulated pairs  $\{\widehat{\theta}_{\text{true},k}, \widehat{D}_k\}$ . The red lines indicate the ideal one-to-one relation  $x = y$ .

relevant), but restricting the evaluation to fewer points  $\widehat{\theta}_{\text{true}} \in [\theta_{\text{min}} + \Delta\theta/2, \theta_{\text{max}} - \Delta\theta/2]$ , where  $\theta_{\text{min}}$  (resp.  $\theta_{\text{max}}$ ) is the lower (resp. upper) bound of the parameter prior,  $\Delta\theta$  represents  $\sim 5\%$  of the prior size, and we “mask” posterior samples accordingly by removing samples outside this updated prior range. As shown in Figure 5, the resulting calibration curve is closer to identity, emphasizing that this prior problem can be solved by (i) training on a broader prior, (ii) restricting the posterior to a tighter prior range, chosen to match the analysis requirement.

Additionally, to test not only the marginalized but the joint posterior, we compute an alternative ECP quantity by using the TARP method (Tests of Accuracy with Random Points, Lemos et al. 2023a), shown in Figure 5, also close to identity, ensuring a good calibration with respect to this metric.

Although they do not guarantee the full validity of the posterior estimation, these tests are effective for detecting potential miscalibration, and all are successfully passed here.

### 3.3. Cosmological analysis: internal validation

Given the configuration `count_Nm`, and considering 500 pairs  $\{\widehat{\theta}_{\text{true},k}, \widehat{D}_k\}$ , we compute the estimated posterior mean  $E[\widehat{\theta}_k | \widehat{D}_k]$  that we compare to the true values  $\widehat{\theta}_{\text{true},k}$  in Figure 6. This consistency test shows that the recovered cosmological parameters are efficiently recovered from the posterior—with some scatter around the true value – with no strong apparent bias.

We study now the shape of the posterior, for that we generate 500 simulations at the same fiducial parameter values (in Table 1). By averaging the data vector over these realizations, we obtain an effectively noiseless data vector, which we use to perform consistency tests of the Bayesian inference. Figure 7 shows the resulting posterior distributions<sup>16</sup> (using `count_Nm`, or `count_Nm`) for the six parameters (the best fits are reported in Table G). In all cases, we find good agreement between the inferred posteriors and the fiducial parameter values, the latter

lying within the  $1\sigma$  region of each posterior distribution, as expected from the test in Figure 6.

As mentioned before, it is possible that cluster number counts of Capish simulations display one or more empty bins, making the computation of the mean mass impossible (that is why we choose the alternative lensing mass statistics). We explore in Appendix C what is the effect of removing the simulations that contain at least one empty cluster-count bin in the training. In this case,  $\log_{10} M_{kl}$  can be computed and then used in the NDE training. In Figure C.1, we show the fraction of non-removed objects after masking over empty count bins, displaying an inhomogeneous shape over the prior space (with  $\sim 40\%$  remaining simulations in the bottom left corner of the prior region). This masking induces a complex, implicit prior on the posterior and breaks the desired transparency of the pipeline to empty bins, and shifts the posterior (as shown in Figure C.2). This confirms that the alternative summary statistics Nm in Eq. (24) is particularly reliable for this task.

We test how the selection-bias parameter  $\rho$  in Eq. (12) – which quantifies the correlation between observed weak-lensing masses and optical richness – impacts cosmological parameter constraints. To this end, we adopt a different noise model than in previous analyses: instead of applying lensing-mass scatter to the stacked mass, the scatter is applied to individual lensing mass measurements. As a baseline, we first train a new `count_Nm` NDE with  $\rho$  being fixed. We then train a second `count_Nm` NDE that includes  $\rho \sim \mathcal{U}(-0.2, 0.2)$ . The resulting posterior samples, applied to the noiseless data vector (computed with  $\rho = 0$ ), are shown in Figure 8 (left panel), marginalized over the parameters  $\mu_0^\lambda$ ,  $\mu_m^\lambda$ ,  $\mu_z^\lambda$ , and  $\sigma_{\ln\lambda,\text{int}}$ . Allowing  $\rho$  to vary leads to slightly broader constraints on  $\sigma_8$ , revealing a negative correlation between the selection-bias parameter and  $\sigma_8$ , and keeping the constraints on  $\Omega_m$  unchanged. This example illustrates Capish incorporates the effect of lensing mass-richness correlation, and that, for the considered prior and current parametrization for  $\rho$ , including selection bias does not modify significantly the inference of cosmological parameters.

<sup>16</sup> Posteriors are displayed with GetDist (Lewis 2025).

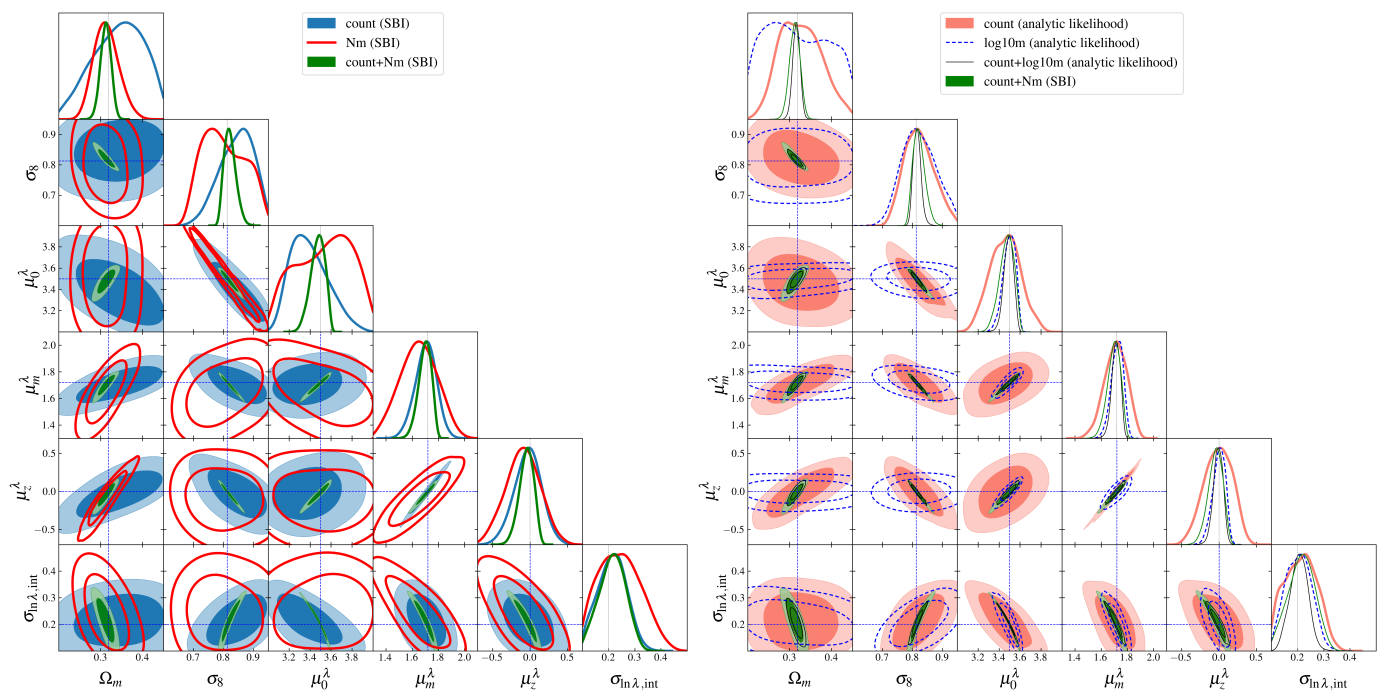


**Fig. 7.** Left: posterior distributions obtained from the trained posterior generator for the three configurations count, Nm, and count\_Nm. Right: corresponding posteriors from the analytic likelihood approach, sampled with MCMC for count, log10m, and count\_log10m (the SBI count\_Nm results are overplotted for comparison).

### 3.4. Cosmological analysis: comparison to the likelihood-based approach

In this subsection we show how the SBI posteriors compare to the posteriors obtained from an analytic likelihood-based approach.

The elements for the likelihood-based approach are detailed in Appendix E; we define a Gaussian cluster abundance likelihood  $\mathcal{L}_{\text{BLC}}^{\text{Gauss-SN+SSC}}$  in Eq. (E.2) accounting for the Poisson noise (Poisson 1837) and SSC (Hu & Kravtsov 2003). For the mean lensing mass likelihood  $\mathcal{L}_{M_{\text{WL}}}$ , we adopt a Gaussian model in Eq. (E.4) for the logarithm of stacked cluster masses, where the covariance is taken to be diagonal. Its diagonal components (i.e., the dispersion of each stacked mass) are computed assuming a Fisher-like approach on an NFW (Navarro et al. 1997) profile model, accounting for the shape noise and shot noise of source galaxies, and the total number of clusters within the stack.

We draw samples from the parameter posterior distribution with the emcee package (Foreman-Mackey et al. 2013) given by the Bayes theorem  $\mathbb{P}(\theta | \text{data}) \propto \mathcal{L}_{\text{tot}}(\text{data} | \theta) \times \pi(\theta)$ , where  $\pi(\theta)$  is the prior distribution mentioned earlier. The results are shown in the right panel of Figure 7; The likelihood-based constraints are consistent with the fiducial parameters, showcasing that the simulation-based noiseless Capish data vectors are not biased between the two methods. The combined constraints and count-only show a comparable shape to the SBI results (left panel of Figure 7), whereas the likelihood-based log10m constraints are very different than the Nm approach, since not the same information is encoded between the two statistics. When combined with counts, however, the discrepancy between SBI and the likelihood-based approach decreases, since the combined constraints show roughly similar posterior widths and correlations as those inferred by SBI. However, we see that likelihood-based error bars are slightly smaller, which we expect is from a series of effects; in the likelihood-based approach, we adopt

a fixed covariance matrices<sup>17</sup> for the lensing masses and cluster counts (to speed up the calculations), whereas in the SBI approach, the covariance can vary across simulations. Our implementation of the likelihood-based approach neglects correlation between probes, which will tighten parameter posterior and Capish accounts for a sampling dispersion (the intrinsic variation of the mean mass in each richness-redshift bins due to the variation of the number of clusters), which is absent from the likelihood-based approach (the error bars are computed as  $\sigma_{\text{WLgal}}/\sqrt{N}$ , where  $N$  is the cluster count at fiducial values). Moreover, the likelihood-based approach assumes variables are Gaussian, whereas Capish will account for any non-gaussian noise in our forward model. Given these effects, it is expected that Capish has slightly broader posteriors than the likelihood based approach.

### 3.5. Cosmological analysis with external simulated datasets

As a final validation, we apply our trained posterior generator to the Euclid Flagship simulation (Euclid Collaboration et al. 2025)<sup>18</sup>. Flagship is a large-scale mock galaxy catalogue designed to support the scientific exploitation of ESA's Euclid mission. The simulation was run using the PKDGRAV3 code (Potter et al. 2017) under a flat- $\Lambda$ CDM cosmology, with cosmological parameters close to those inferred by Planck Collaboration et al. (2016). A light cone extending to  $z = 3$  was generated on the fly, covering one octant of the sky (approximately 5,157 deg<sup>2</sup>). Dark matter halos were identified using the rockstar algorithm (Behroozi et al. 2013). From these halos, we construct a Flagship-based cluster catalogue by assigning optical richnesses  $\lambda_{\text{obs}}$  using the fiducial parameters listed in Table 1 for the cluster mass–richness relation in Eq. (13). Lensing masses  $m_{\text{WL}}$  are

<sup>17</sup> Computed at the fiducial cosmology and scaling relation parameters.

<sup>18</sup> <https://cosmohub.pic.es>

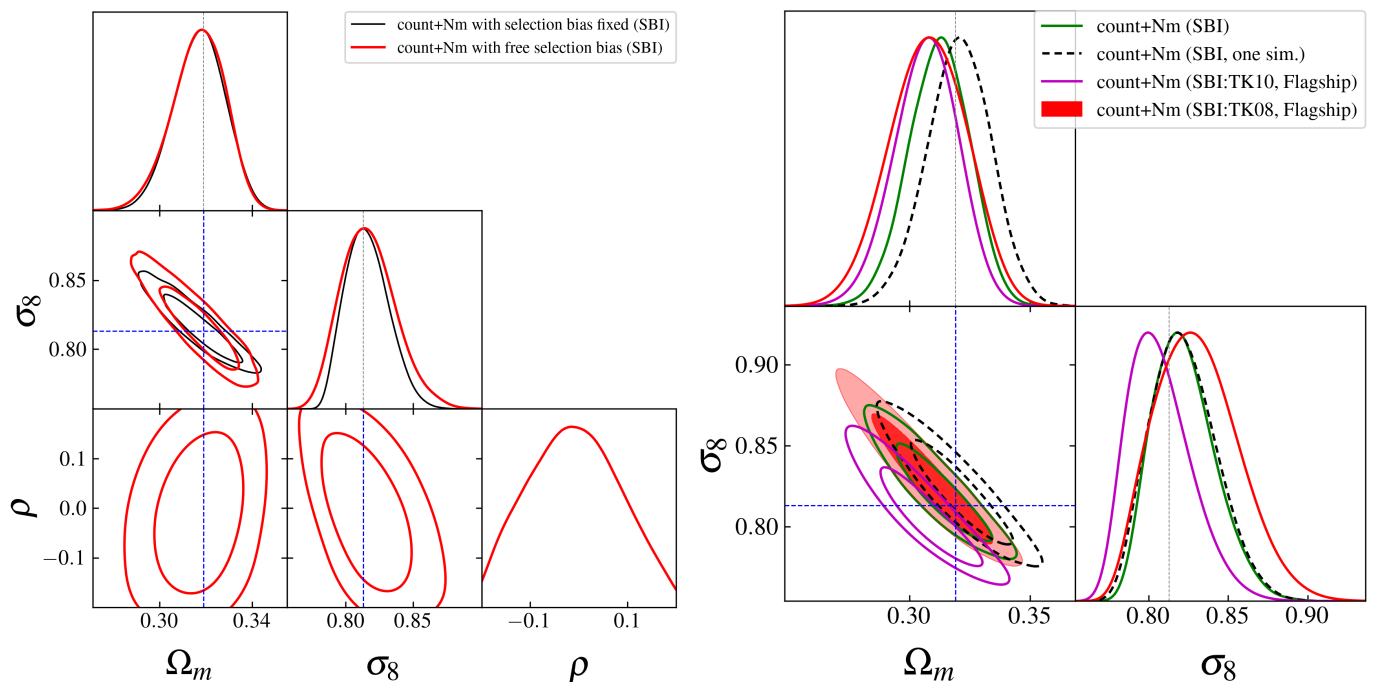


**Fig. 8.** Left: Posterior distributions obtained on a noiseless data vector with the count\_Nm setup; the blue posterior is obtained by training on only 6 parameters, and the red is trained adding the lensing mass–richness correlation parameter  $\rho$ . Right: Posterior distributions from different SBI posterior generators: (i) count\_Nm applied to the noiseless data vector, (ii) count\_log10m with empty counts masked applied to the noiseless data vector, (iii) count\_Nm applied to a single fiducial simulation, and (iv) count\_Nm applied to the Flagship simulation with richness drawn from Capish.

generated without scatter, with stochasticity applied only at the stacked level when constructing the cluster count and lensing mass matrices. Figure 8 (right panel) shows the posterior distributions for the cosmological parameters ( $\Omega_m, \sigma_8$ ) obtained with our SBI framework using three different data vectors: (i) a noiseless data vector, (ii) a single Capish simulation, and (iii) the Flagship simulation with Capish-like richnesses. In the case of the single Capish realization, the posterior is slightly shifted, primarily due to statistical noise in the data. For the SBI applied to the Flagship catalogue when using the Tinker et al. (2010) [TK10], we find a good agreement with the fiducial cosmology for the marginalized posteriors, but still with a  $\sim 2\sigma$  tension in the  $\Omega_m, \sigma_8$  plane. This residual tension can be attributed to the fact that we performed our training assuming the Tinker et al. (2010) halo mass function, which is different from the effective mass function measured in the Flagship simulation (Euclid Collaboration et al. 2025), whose underlying halo mass function was found to be closer to the Tinker et al. (2008) [TK08] implementation (see Appendix F). We repeat the training this time using the TK08 halo mass function, which enables us to recover the good cosmological parameters with no significant tension (below  $1\sigma$ ). In practice, the underlying halo mass function is unknown, such as incorporating additional nuisance parameters in the training, accounting for uncertainties in the halo mass function calibration (Wu et al. 2010; Cunha & Evrard 2010; Artis et al. 2021) could help mitigate this discrepancy.

#### 4. Conclusions

In this work, we have presented Capish, a simulation-based inference framework for the cosmological analysis of galaxy cluster datasets. Rather than relying on explicit likelihood modelling, Capish learns posterior distributions directly from forward-modelled cluster observables — specifically cluster number

counts and mean weak-lensing masses in richness–redshift bins — naturally capturing non-Gaussian features of the data that analytic likelihood approaches cannot. The forward model incorporates Poisson sampling noise and super-sample covariance using log-normal variables, extending the approach of Payerne et al. (2024), as well as lensing mass scatter, selection effects through purity and selection biases, and an alternative lensing mass statistic — given by the product of count and mean lensing mass — to regularise the neural density estimator training. Capish performs posterior inference using neural posterior estimation within the sbi package (Lin et al. 2023).

The code has been validated by comparing its outputs at fiducial values against analytical predictions, confirming that the simulated cluster counts accurately reproduce the expected SSC variance. The flexibility of the selection function implementation has been tested, and the impact of lensing mass–richness covariance on recovered masses has been assessed. Bayesian coverage tests indicate that the posteriors are unbiased and provide robust uncertainty estimates for both cosmological and scaling-relation parameters. We have also examined how the effective lensing mass–richness correlation parameter (Wu et al. 2022; Zhang et al. 2024), one of the major systematic effects in cosmology with optically-selected clusters, propagates into the cosmological posteriors. Comparisons with likelihood-based analyses (Payerne et al. 2023) show good overall agreement, with the broader SBI posteriors reflecting the increased realism of the forward model. As a final validation, Capish has been applied to the Euclid Flagship dataset (Euclid Collaboration et al. 2025) with Capish-assigned richnesses, recovering the Flagship cosmological parameters within  $1\sigma$ .

This framework offers a flexible and robust alternative for analyses of surveys such as DES, Euclid (Laureijs et al. 2011), and LSST (LSST Science Collaboration et al. 2009), and we pro-

pose it as a test bench for validating traditional likelihood-based cosmological pipelines and assessing their internal consistency.

*Acknowledgements.* We gratefully acknowledge support from the CNRS/IN2P3 Computing Center (Lyon - France) for providing computing and data-processing resources needed for this work. We thank the developers and maintainers of the following software tools used in this work: *sbi* (Lin et al. 2023), *NumPy* (van der Walt et al. 2011), *SciPy* (Jones et al. 2001), *Matplotlib* (Hunter 2007), *GetDist* (Lewis 2025), *emcee* (Foreman-Mackey et al. 2013), *Jupyter* (Kluyver et al. 2016).

## References

- Abbott, T., Aguena, M., Alarcon, A., et al. 2020, *Phys. Rev. D*, 102, 023509
- Abbott, T. M. C., Aguena, M., Alarcon, A., et al. 2025, *Phys. Rev. D*, 112, 083535
- Ade, P., Aghanim, N., Armitage-Caplan, C., et al. 2016, *A&A*, 594, A24
- Aguena, M., Benoist, C., da Costa, L. N., et al. 2021, *MNRAS*, 502, 4435
- Aguena, M. & Lima, M. 2018, *Phys. Rev. D*, 98, 123529
- Anbajagane, D., Evrard, A. E., Farahi, A., et al. 2020, *MNRAS*, 495, 686
- Artis, E., Melin, J.-B., Bartlett, J. G., & Murray, C. 2021, *A&A*, 649, A47
- Aymerich, G., Douspiss, M., Pratt, G. W., et al. 2024, *A&A*, 690, A238
- Bartelmann, M. & Schneider, P. 2001, *Phys. Rep.*, 340, 291
- Bartlett, J. G. 1997, *Astronomical Society of the Pacific Conference Series*, 126, 365
- Becker, M. R. & Kravtsov, A. V. 2011, *ApJ*, 740, 25
- Behroozi, P. S., Wechsler, R. H., & Wu, H.-Y. 2013, *ApJ*, 762, 109
- Bellagamba, F., Roncarelli, M., Maturi, M., & Moscardini, L. 2018, *MNRAS*, 473, 5221
- Bocquet, S., Grandis, S., Bleem, L. E., et al. 2024, *Phys. Rev. D*, 110, 083510
- Bocquet, S., Grandis, S., Krause, E., et al. 2025, *Phys. Rev. D*, 111, 063533
- Cerardi, N., Pierre, M., Lanusse, F., & Corap, X. 2025, *A&A*, 701, A110
- Chang, C., Jarvis, M., Jain, B., et al. 2013, *MNRAS*, 434, 2121
- Chaubal, P. S., Reichardt, C. L., Gupta, N., et al. 2022, *ApJ*, 931, 139
- Coles, P. & Jones, B. 1991, *MNRAS*, 248, 1
- Costanzi, M., Rozo, E., Rykoff, E. S., et al. 2019, *MNRAS*, 482, 490
- Costanzi, M., Saro, A., Bocquet, S., et al. 2021, *Phys. Rev. D*, 103, 043522
- Cunha, C. E. & Evrard, A. E. 2010, *Phys. Rev. D*, 81, 083509
- Despali, G., Giocoli, C., Angulo, R. E., et al. 2016, *MNRAS*, 456, 2486
- Duffy, A. R., Schaye, J., Kay, S. T., & Dalla Vecchia, C. 2008, *MNRAS*, 390, L64
- Euclid Collaboration, Castander, F. J., Fosalba, P., et al. 2025, *A&A*, 697, A5
- Evrard, A. E., Arnault, P., Huterer, D., & Farahi, A. 2014, *MNRAS*, 441, 3562
- Farahi, A., Evrard, A. E., McCarthy, I., Barnes, D. J., & Kay, S. T. 2018, *MNRAS*, 478, 2618
- Foreman-Mackey, D., Hogg, D. W., Lang, D., & Goodman, J. 2013, *PASP*, 125, 306
- Fumagalli, A., Costanzi, M., Saro, A., Castro, T., & Borgani, S. 2023, *arXiv e-prints*, arXiv:2310.09146
- Fumagalli, A., Saro, A., Borgani, S., et al. 2021, *A&A*, 652, A21
- Gatti, M., Campailla, G., Jeffrey, N., et al. 2025, *Phys. Rev. D*, 111, 063504
- Ghirardini, V., Bulbul, E., Artis, E., et al. 2024, *A&A*, 689, A298
- Gouyou Beauchamps, S., Lacasa, F., Tutusaus, I., et al. 2022, *A&A*, 659, A128
- Graham, M. L., Connolly, A. J., Ivezić, Ž., et al. 2018, *AJ*, 155, 1
- Grandis, S., Ghirardini, V., Bocquet, S., et al. 2024, *A&A*, 687, A178
- Gruen, D., Seitz, S., Becker, M. R., Friedrich, O., & Mana, A. 2015, *MNRAS*, 449, 4264
- Hasselfield, M., Hilton, M., Marriage, T. A., et al. 2013, *J. Cosmology Astropart. Phys.*, 2013, 008
- Hernández-Martín, B., Schrabback, T., Hoekstra, H., et al. 2020, *A&A*, 640, A117
- Hoekstra, H. 2001, *A&A*, 370, 743
- Hoekstra, H. 2003, *MNRAS*, 339, 1155
- Hu, W. & Kravtsov, A. V. 2003, *ApJ*, 584, 702
- Hunter, J. D. 2007, *Computing in Science and Engineering*, 9, 90
- Jeffrey, N., Alsing, J., & Lanusse, F. 2021, *MNRAS*, 501, 954
- Jones, E., Oliphant, T., & Peterson, P. 2001
- Kluyver, T., Ragan-Kelley, B., Pérez, F., et al. 2016, in *IOS Press*, 87–90
- Kosiba, M., Cerardi, N., Pierre, M., et al. 2025, *A&A*, 693, A46
- Lacasa, F., Aubert, M., Baratta, P., et al. 2023, *A&A*, 671, A115
- Lacasa, F. & Grain, J. 2019, *A&A*, 624, A61
- Lacasa, F., Lima, M., & Aguena, M. 2018, *A&A*, 611, A83
- Laureijs, R., Amiaux, J., Arduini, S., et al. 2011, *arXiv e-prints*, arXiv:1110.3193
- Lee, B. E., Le Brun, A. M. C., Haq, M. E., et al. 2018, *MNRAS*, 479, 890
- Lee, E., Battye, R., & Bolliet, B. 2024, *arXiv e-prints*, arXiv:2403.19542
- Lemos, P., Coogan, A., Hezaveh, Y., & Perreault-Levasseur, L. 2023a, 40th International Conference on Machine Learning, 202, 19256
- Lemos, P., Parker, L. H., Hahn, C., et al. 2023b, in *Machine Learning for Astrophysics*, 18
- Lesci, G. F., Marulli, F., Moscardini, L., et al. 2025, *A&A*, 703, A25
- Lesci, G. F., Marulli, F., Moscardini, L., et al. 2022, *A&A*, 659, A88
- Lewis, A. 2025, *J. Cosmology Astropart. Phys.*, 2025, 025
- Lin, K., von Wietersheim-Kramsta, M., Joachimi, B., & Feeney, S. 2023, *MNRAS*, 524, 6167
- LSST Science Collaboration, Abell, P. A., Allison, J., et al. 2009, *arXiv e-prints*, arXiv:0912.0201
- Mantz, A., Allen, S. W., Ebeling, H., & Rapetti, D. 2008, *MNRAS*, 387, 1179
- Mantz, A., Allen, S. W., Rapetti, D., & Ebeling, H. 2010, *MNRAS*, 406, 1759
- Mantz, A. B. 2019, *MNRAS*, 485, 4863
- Mantz, A. B., von der Linden, A., Allen, S. W., et al. 2015, *MNRAS*, 446, 2205
- McClintock, T., Varga, T. N., Gruen, D., et al. 2019, *MNRAS*, 482, 1352
- Melchior, P., Gruen, D., McClintock, T., et al. 2017, *MNRAS*, 469, 4899
- Mistele, T. & Durakovic, A. 2024, *OJAp*, 7, 120
- Murrata, R., Oguri, M., Nishimichi, T., et al. 2019, *PASJ*, 71, 107
- Murray, C., Bartlett, J. G., Artis, E., & Melin, J.-B. 2022, *MNRAS*, 512, 4785
- Murray, C., Combet, C., Payerne, C., & Ricci, M. 2025, *A&A*, 697, A141
- Navarro, J. F., Frenk, C. S., & White, S. D. M. 1997, *ApJ*, 490, 493
- Nord, B., Stanek, R., Rasia, E., & Evrard, A. E. 2008, *MNRAS*, 383, L10
- Nyarko Nde, T., Wu, H.-Y., Cao, S., et al. 2025, *arXiv e-prints*, arXiv:2510.00753
- Oguri, M., Takada, M., Okabe, N., & Smith, G. P. 2010, *MNRAS*, 405, 2215
- Park, Y., Sunayama, T., Takada, M., et al. 2023, *MNRAS*, 518, 5171
- Payerne, C., Murray, C., Combet, C., et al. 2023, *MNRAS*, 520, 6223
- Payerne, C., Murray, C., Combet, C., & Penna-Lima, M. 2024, *MNRAS*, 532, 381
- Payerne, C., Zhang, Z., Aguena, M., et al. 2025, *A&A*, 700, A34
- Penna-Lima, M., Bartlett, J. G., Rozo, E., et al. 2017, *A&A*, 604, A89
- Penna-Lima, M., Makler, M., & Wuensche, C. A. 2014, *J. Cosmology Astropart. Phys.*, 2014, 039
- Planck Collaboration, Ade, P. A. R., Aghanim, N., et al. 2016, *A&A*, 594, A24
- Poisson, S. D. 1837, *Bachelier, Imprimeur-Librairie*
- Potter, D., Stadel, J., & Teyssier, R. 2017, *COMPAC*, 4, 2
- Prat, J., Gatti, M., Doux, C., et al. 2026, *MNRAS*, 545, staf2152
- Pratt, G. W., Arnaud, M., Biviano, A., et al. 2019, *Space Sci. Rev.*, 215, 25
- Regamey, M., Eckert, D., Seppi, R., et al. 2025, *arXiv e-prints*, arXiv:2506.05457
- Reza, M., Zhang, Y., Avestruz, C., et al. 2024, *arXiv e-prints*, arXiv:2409.20507
- Reza, M., Zhang, Y., Nord, B., et al. 2022, in *Machine Learning for Astrophysics*, 20
- Roza, E., Evrard, A. E., Rykoff, E. S., & Bartlett, J. G. 2014, *MNRAS*, 438, 62
- Roza, E., Wechsler, R. H., Rykoff, E. S., et al. 2010, *ApJ*, 708, 645
- Rykoff, E. S., Roza, E., Busha, M. T., et al. 2014, *ApJ*, 785, 104
- Sáez-Casares, I., Calabrese, M., Bianchi, D., et al. 2026, *arXiv e-prints*, arXiv:2601.03894
- Salcedo, A. N., Wu, H.-Y., Roza, E., et al. 2024, *Phys. Rev. Lett.*, 133, 221002
- Salvati, L., Saro, A., Bocquet, S., et al. 2022, *ApJ*, 934, 129
- Saro, A., Bocquet, S., Roza, E., et al. 2015, *MNRAS*, 454, 2305
- Sehgal, N., Trac, H., Acquaviva, V., et al. 2011, *ApJ*, 732, 44
- Sheldon, E. S., Johnston, D. E., Frieman, J. A., et al. 2004, *AJ*, 127, 2544
- Shirasaki, M. & Takada, M. 2018, *MNRAS*, 478, 4277
- Sommer, M. W., Schrabback, T., Applegate, D. E., et al. 2022, *MNRAS*, 509, 1127
- Sunayama, T., Miyatake, H., Sugiyama, S., et al. 2024, *Phys. Rev. D*, 110, 083511
- Sunayama, T., Park, Y., Takada, M., et al. 2020, *MNRAS*, 496, 4468
- Takada, M. & Spergel, D. N. 2014, *MNRAS*, 441, 2456
- Tejero-Cantero, A., Boeltis, J., Deistler, M., et al. 2020, *The Journal of Open Source Software*, 5, 2505
- Tinker, J., Kravtsov, A. V., Klypin, A., et al. 2008, *ApJ*, 688, 709
- Tinker, J. L., Robertson, B. E., Kravtsov, A. V., et al. 2010, *ApJ*, 724, 878
- To, C., Krause, E., Roza, E., et al. 2021, *Phys. Rev. Lett.*, 126, 141301
- To, C.-H., Krause, E., Chang, C., et al. 2025, *Phys. Rev. D*, 112, 063537
- Umetsu, K. 2020, *A&A Rev.*, 28, 7
- van der Walt, S., Colbert, S. C., & Varoquaux, G. 2011, *Computing in Science and Engineering*, 13, 22
- Varga, T. N., DeRose, J., Gruen, D., et al. 2019, *MNRAS*, 489, 2511
- von der Linden, A., Mantz, A., Allen, S. W., et al. 2014, *MNRAS*, 443, 1973
- von Wietersheim-Kramsta, M., Lin, K., Tessore, N., et al. 2025, *A&A*, 694, A223
- Wen, D., Kembell, A. J., & Saslaw, W. C. 2020, *ApJ*, 890, 160
- Wright, A. H., Hildebrandt, H., van den Busch, J. L., & Heymans, C. 2020, *A&A*, 637, A100
- Wu, H.-Y., Costanzi, M., To, C.-H., et al. 2022, *MNRAS*, 515, 4471
- Wu, H.-Y., Weinberg, D. H., Salcedo, A. N., Wibking, B. D., & Zu, Y. 2019, *MNRAS*, 490, 2606
- Wu, H.-Y., Zentner, A. R., & Wechsler, R. H. 2010, *ApJ*, 713, 856
- Zhang, Y., Jeltama, T., Hollowood, D. L., et al. 2019, *MNRAS*, 487, 2578
- Zhang, Z., Farahi, A., Nagai, D., et al. 2024, *MNRAS*, 530, 3127
- Zhang, Z., Wu, H.-Y., Zhang, Y., et al. 2023, *MNRAS*, 523, 1994–2013
- Zhou, C., Wu, H.-Y., Salcedo, A. N., et al. 2024, *Phys. Rev. D*, 110, 103508
- Zubeldia, Í., Bolliet, B., Challinor, A., & Handley, W. 2025, *Phys. Rev. D*, 112, 083536
- Zubeldia, Í. & Challinor, A. 2019, *MNRAS*, 489, 401

## Appendix A: Error model for lensing mass

For a single halo with mass  $m$  and redshift  $z$ , the dispersion of the cluster lensing mass proxy  $\sigma_M$  is obtained from

$$F_{MM} = \int_{R_{\min}}^{R_{\max}} \sigma_{\Delta\Sigma}^{-2}(R) \left( \frac{\partial \Delta\Sigma(R)}{\partial M} \right)^2 dR, \quad (\text{A.1})$$

where  $\Delta\Sigma(R) = \Delta\Sigma_{\text{NFW}}(R|M, c)$  is the predicted excess surface density for an NFW (Navarro et al. 1997) halo of mass  $m$ , concentration  $c$  given by the (Duffy et al. 2008) concentration mass-relation. The per-radius dispersion of the excess surface density profile entering Eq. (A.1) has several sources listed in Section 2.2. We focus on the shape and shot noise of the source galaxy sample, given by

$$\sigma_{\Delta\Sigma}^2(R) = \frac{\Sigma_{\text{crit}}^2(z_{\text{cl}}) \sigma_{\epsilon}^2}{n_{\text{gal}}^{\text{bgd}}(z_{\text{cl}}) 2\pi R}, \quad (\text{A.2})$$

where  $\sigma_{\epsilon}$  is the intrinsic galaxy shape noise and  $n_{\text{gal}}^{\text{bgd}}(z)$  is the surface density of background galaxies behind a cluster at redshift  $z$ , given by

$$n_{\text{gal}}^{\text{bgd}}(z_{\text{cl}}) = \bar{n}_{\text{gal}} \frac{\int_{z_{\text{cl}}+0.2}^{\infty} n_{\text{gal}}(z_s) dz_s}{\int_0^{\infty} n_{\text{gal}}(z_s) dz_s}. \quad (\text{A.3})$$

where the Chang et al. (2013) normalized redshift distribution is given by

$$n_{\text{gal}}(z_s) \propto z_s^{\alpha_{\text{gal}}} \exp\left(-\left(\frac{z_s}{z_{\text{gal}}^0}\right)^{\beta_{\text{gal}}}\right), \quad (\text{A.4})$$

where  $\alpha_{\text{gal}}, \beta_{\text{gal}}$  and  $z_{\text{gal}}^0$  are given in Table 1. The effective critical surface density is averaged over the source redshift distribution  $n(z_s)$ , such as

$$\Sigma_{\text{crit}}^{-2}(z_{\text{cl}}) = \frac{\int_{z_{\text{cl}}+0.2}^{\infty} n_{\text{gal}}(z_s) \Sigma_{\text{crit}}^{-2}(z_{\text{cl}}, z_s) dz_s}{\int_{z_{\text{cl}}+0.2}^{\infty} n_{\text{gal}}(z_s) dz_s}. \quad (\text{A.5})$$

Then, we get that

$$\sigma_{\text{WL}}(m, z) = \frac{\sqrt{F_{MM}^{-1}}}{\ln(10)m}, \quad (\text{A.6})$$

represented in Figure A.1 as a function of mass and redshift.

## Appendix B: Alternative interpretation of completeness

In Section 2.2, we found that a completeness  $c(m, z) < 1$  (given by the ratio between detected halos and the underlying halo population) emerges when a richness cut is applied to the detected cluster catalog. It is also possible to interpret completeness as the portion of the underlying dark matter halo population that is systematically missing from our dataset (Mantz et al. 2010; Mantz 2019), even for a pure sample, with no richness cut applied (all clusters are selected). Following Agüena & Lima (2018); Payerne et al. (2025); Lesci et al. (2022); Lesci et al. (2025), the observed cluster number counts per interval of halo mass, redshift, and richness can be written as

$$\frac{\partial^4 N(m, z, \lambda_{\text{obs}}, z_{\text{obs}})}{\partial \lambda_{\text{obs}} \partial m \partial z_{\text{obs}} \partial z} = \frac{\partial^2 N(m, z)}{\partial m \partial z} \frac{c(m, z)}{p(\lambda_{\text{obs}}, z_{\text{obs}})} \times P(\lambda_{\text{obs}} | m, z) P(z_{\text{obs}} | z). \quad (\text{B.1})$$

In this formalism, completeness is treated independently of purity and mass-richness relation effects, in contrast to the current implementation in Capish (see Section 2.2). We could consider the completeness parametrization (Agüena & Lima 2018)

$$c(m, z) = \frac{(m/m_c)^{n_{\text{comp}}(z)}}{1 + (m/m_c)^{n_{\text{comp}}(z)}}. \quad (\text{B.2})$$

From a simulation point of view, for each halo with mass and redshift  $m, z$ , we generate  $u \sim U(0, 1)$ , if  $u > c(m, z)$ , the halo is removed from the catalog. Along with the implementation of purity in Section 2.2, completeness reproduces the Eq. (B.1).

## Appendix C: Dealing with empty bins

In Figure C.1, we show the ratio map between (i) the full set of 30,000 parameter samples  $\theta_k$  drawn from the priors defined in Section 3.2 and (ii) the same parameter samples after masking those that produce binned cluster counts with at least one empty bin. We find that most of the excluded samples are concentrated in the lower-left region of the two-dimensional parameter space, corresponding to low values of  $\Omega_m$  and  $\sigma_8$ .

This selective removal affects the posterior training by effectively imposing a smooth prior in the low- $\Omega_m$ -low- $\sigma_8$  region. In Figure C.2, we show the posterior distributions obtained for the idealized data vector using three configurations: count\_masked, log10m, and count\_log10m, where the counts are masked, and the mean logarithmic mass can therefore be computed. Compared to the unmasked case using the appropriate Nm statistics, the resulting posteriors exhibit a small but noticeable shift.

## Appendix D: Computing probability coverage over the full SBI training prior

As discussed in Section 3.2, Bayesian robustness tests are crucial to assess the performance and reliability of NDE for cosmological parameter inference. For each of the 60,000 simulations drawn from the prior defined in Section 3.2, we draw 5000 samples from the corresponding posterior estimates to obtain a  $\gamma$ -credible set, for  $\gamma \in [0, 1]$ . The fraction of sets that contain the true parameter converges to the Expected Coverage Probability (ECP)  $p_{\gamma}$ , which calibration curves are shown in Figure D.1. We observe a tendency toward overconfidence (empirical coverage  $p_{\gamma}$  lower than nominal coverage  $\gamma$ ), which can be mitigated by evaluating the ECP with the posterior estimate restricted to a tighter range.

## Appendix E: Analytical likelihood approach

### Appendix E.1: Count likelihood

The analytical prediction for the cluster number count is given by (Payerne et al. 2023)

$$N_{ij} = \Omega_S \int_{\lambda_i}^{\lambda_{i+1}} \int_{z_j}^{z_{j+1}} \int_{m_{\min}}^{m_{\max}} dz dm d\lambda_{\text{obs}} P(\lambda_{\text{obs}} | m, z) n_h(m, z). \quad (\text{E.1})$$

In the above equation, we consider the mass-richness relation  $\ln \lambda_{\text{obs}} \sim \mathcal{N}(\langle \ln \lambda_{\text{obs}} | m, z \rangle, \sigma_{\ln \lambda}^2)$ , where  $\langle \ln \lambda_{\text{obs}} | m, z \rangle$  is given in Eq. (13) and  $\sigma_{\ln \lambda}^2$  is given in Eq. (14), no selection function

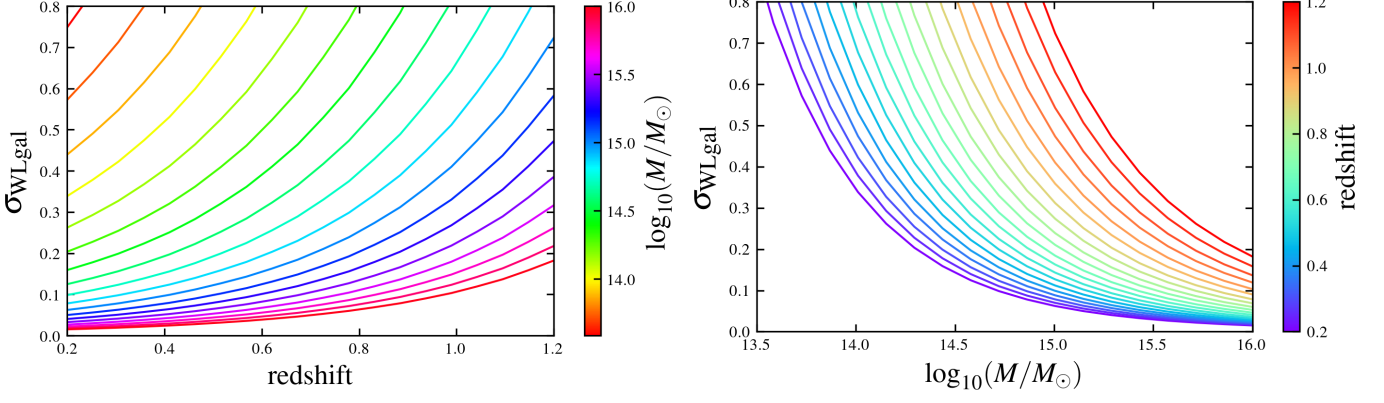


**Fig. A.1.** Left: Dispersion on the  $\log_{10} m_{WL}$  as a function of redshift for different halo mass values. Right: Dispersion on the  $\log_{10} m_{WL}$  as a function of halo mass for different redshift values.

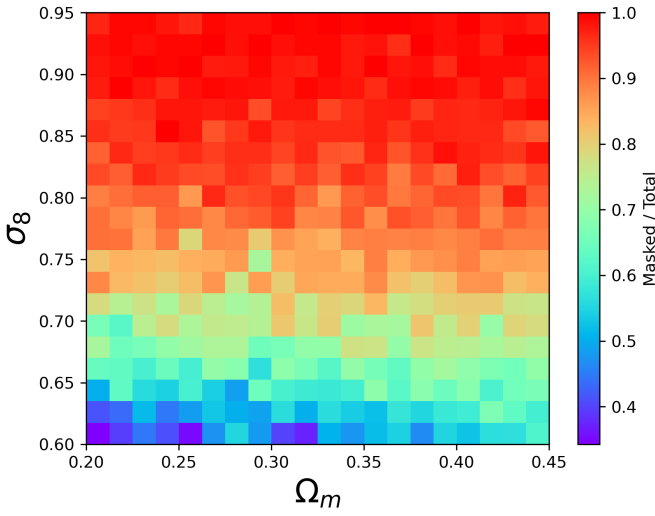


**Fig. C.1.** Ratio between the two-dimensional distribution of sampled parameters in the  $\Omega_m - \sigma_8$  plane and the same distribution after masking simulations that contain at least one empty richness-redshift bin.

and no photometric redshift, i.e.  $z_{true} = z_{phot}$ . We use the Gaussian likelihood given by

$$\mathcal{L}_{BLC}^{\text{Gauss-SN+SSC}} \propto |\Sigma_N|^{-2} \exp \left[ -\frac{1}{2} [N - \widehat{N}]^T \Sigma_N^{-1} [N - \widehat{N}] \right] \quad (\text{E.2})$$

where

$$(\Sigma_N)_{ij,kl} = N_{ij} \delta_{ik}^K \delta_{jl}^K + N_{ij} N_{kl} \langle b \rangle_{ij} \langle b \rangle_{kl} S_{jl}, \quad (\text{E.3})$$

is the binned count covariance (Lacasa et al. 2023). The first term is the Poisson shot noise and the second is the binned SSC contribution, and  $\langle b \rangle_{ij}$  is the average halo bias in the given richness-redshift bin.

### Appendix E.2: Mass likelihood

For the mean weak-lensing mass, we consider the Gaussian likelihood

$$\mathcal{L}_{MWL} \propto |\Sigma_M|^{-2} \exp \left[ -\frac{1}{2} \sum_{ij} \left( \frac{\log_{10}(M_{ij}) - \log_{10}(\widehat{M}_{ij})}{\sigma_{\log_{10} M_{ij}}} \right)^2 \right], \quad (\text{E.4})$$

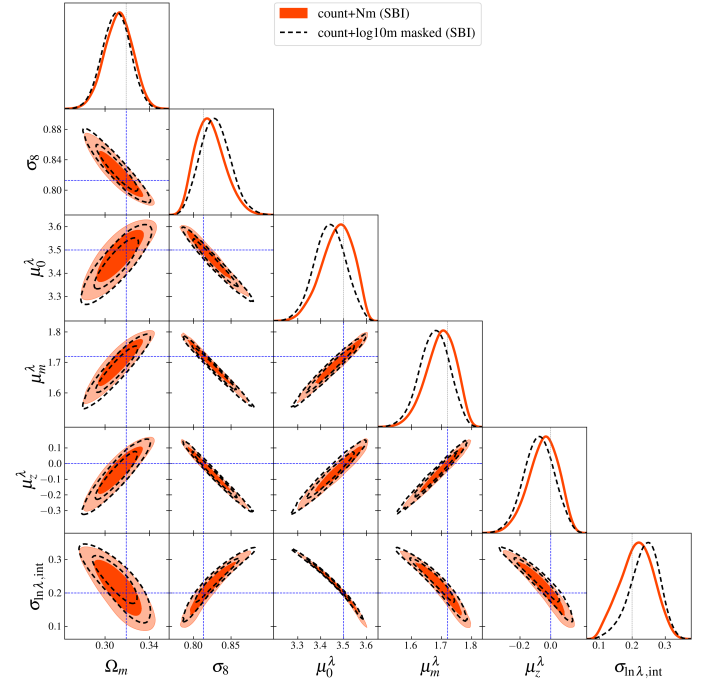


**Fig. C.2.** posterior distributions obtained from the trained posterior generator for the three configurations count, Nm, and count\_Nm, but masking sampled parameters which generated simulations with at least one empty bin.

where  $\widehat{M}_{ij}$  is the observed mean mass in richness-redshift bin  $(i, j)$  and  $\Sigma_{\log_{10} M}$  is the diagonal covariance of  $\log_{10} M$  uncertainties. The theoretical mean mass in each bin is

$$M_{ij}^\Gamma = \frac{\Omega_S}{\widehat{N}_{ij}} \int_{\lambda_i}^{\lambda_{i+1}} \int_{z_j}^{z_{j+1}} \int_{m_{\min}}^{m_{\max}} m^\Gamma W(z) \times P(\lambda_{\text{obs}}|m, z) n_h(m, z) dm d\lambda_{\text{obs}} dz, \quad (\text{E.5})$$

where  $\widehat{N}_{ij}$  is identical to  $N_{ij}$  in Eq. (E.1) with the addition of the window function  $W(z)$ . The uncertainty on the mean logarithmic mass is propagated from the Fisher information of the weak-lensing profile for a single cluster:

$$\sigma_{\log_{10} M_{ij}}(M_{ij}) = \frac{\sigma_M(M_{ij})}{\ln(10) M_{ij}} \frac{1}{\sqrt{\widehat{N}_{ij}}}. \quad (\text{E.6})$$

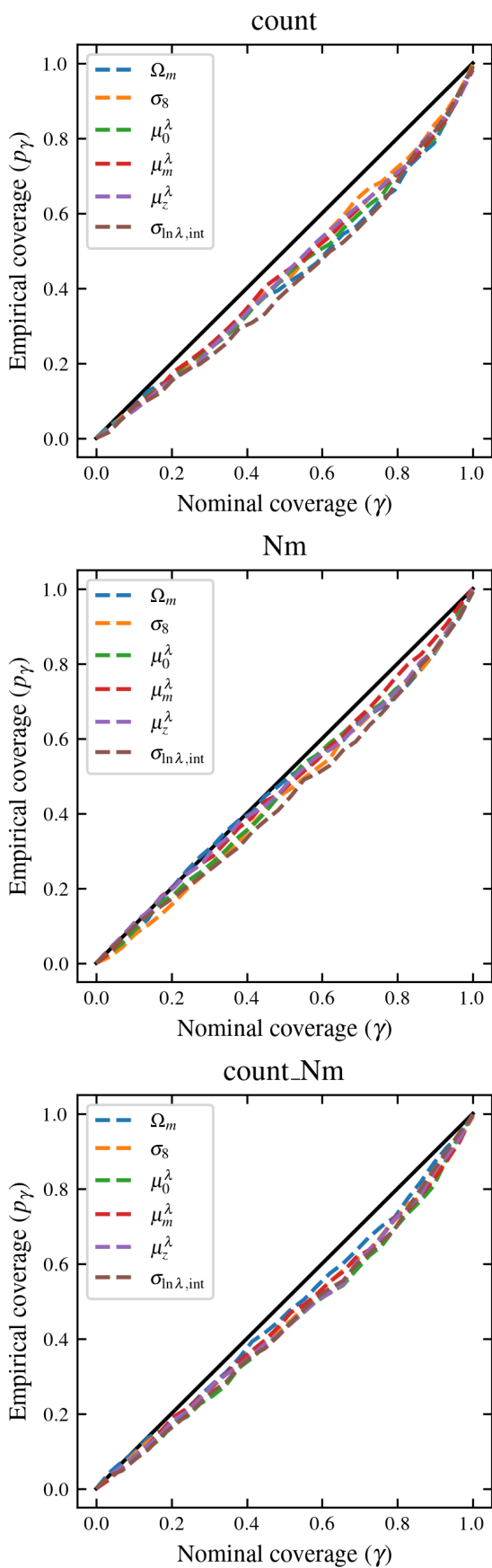


**Fig. D.1.** ECP computed for the three posterior estimates. Top: trained on counts only (count); middle: trained on the product of counts and mean masses (Nm); bottom: trained on the combination of counts and mean masses (count\_Nm). Each panel shows the fraction of true parameter values falling within the corresponding credible intervals, illustrating the calibration of the SBI posteriors.

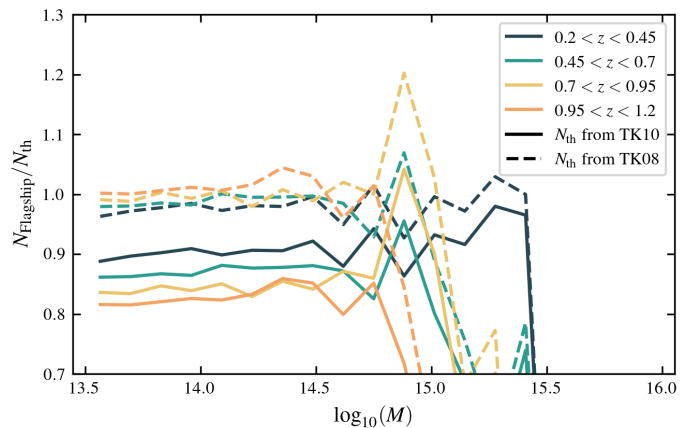


**Fig. F.1.** Halo abundance measured in the *Euclid* Flagship simulation, compared to halo abundance prediction based on Tinker et al. (2010) and Tinker et al. (2008).

The uncertainty on the cluster mass  $\sigma_M$  is obtained from the inverse Fisher matrix constructed for the parameters  $\theta = (M, c, A)$ , where  $c$  is the NFW concentration and  $A$  is a global multiplicative amplitude factor. The Fisher matrix is defined as

$$F_{\alpha\beta} = \int_{R_{\min}}^{R_{\max}} \frac{1}{\sigma_{\Delta\Sigma}^2(R)} \frac{\partial \Delta\Sigma(R)}{\partial \theta_\alpha} \frac{\partial \Delta\Sigma(R)}{\partial \theta_\beta} dR, \quad (\text{E.7})$$

with  $\Delta\Sigma(R) = A \times \Delta\Sigma_{\text{NFW}}(R|m, c)$  the predicted excess surface density for an NFW halo of mass  $M$ , concentration  $c$ , and amplitude  $A$ . The amplitude  $A$  denotes the possible mis-calibration of source photometric redshifts and shape measurement error. The per-radius dispersion of the excess surface density profile  $\sigma_{\Delta\Sigma}^2(R)$  can be modeled as in Eq. (A.2). Gaussian priors with width  $\sigma_\alpha^2$  can be used to constrain better the systematics like  $F_{\alpha\alpha} \rightarrow F_{\alpha\alpha} + 1/\sigma_\alpha^2$ . The covariance matrix is then  $C_{\alpha\beta} = (F^{-1})_{\alpha\beta}$  and  $\sigma_M = \sqrt{C_{MM}}$ . In this work, we put priors of zero width for the amplitude  $A$  and for the concentration  $c$ , to mimic the error model for individual lensing masses in Appendix A (which uses a fixed concentration-mass relation, and  $A = 1$ ).

## Appendix F: Flagship underlying halo mass function

We compute the halo abundance (as described in Section 2.1) and compare it with the abundance of dark matter halos identified in the *Euclid* Flagship simulation. The measured abundance is contrasted with predictions from the halo mass function implementations of Tinker et al. (2010) and Tinker et al. (2008). As shown in Figure F.1, the bias between the simulated and predicted abundances highlights—consistent with Euclid Collaboration et al. (2025)—that the Tinker et al. (2008) formulation provides a better match to the simulated dataset.

## Appendix G: Summary table of cosmological and scaling relation parameter fits

We recap the different constraints on the cosmological parameters  $\Omega_m$  and  $\sigma_8$ , as well as on the scaling-relation parameters, obtained in this work. The first line corresponds to the fiducial values, the second block to the SBI results, and the final block to the analytic likelihood results.

**Table G.1.** Means and  $1\sigma$  dispersions of parameter posteriors for  $\Omega_m, \sigma_8, \mu_0^\lambda, \mu_m^\lambda, \mu_z^\lambda, \sigma_{\ln \lambda, \text{int}}$  obtained in this work. The first block lists the fiducial values, the second lists the SBI constraints, the second block lists analytic-likelihood constraints.

Parameters	$\Omega_m$	$\sigma_8$	$\mu_0^\lambda$	$\mu_m^\lambda$	$\mu_z^\lambda$	$\sigma_{\ln \lambda, \text{int}}$
Fiducial	0.319	0.813	3.5	1.72	0	0.2
count (SBI)	$0.343 \pm 0.058$	$0.845 \pm 0.055$	$3.396 \pm 0.174$	$1.704 \pm 0.078$	$-0.029 \pm 0.176$	$0.214 \pm 0.053$
Nm (SBI)	$0.314 \pm 0.029$	$0.804 \pm 0.068$	$3.533 \pm 0.255$	$1.649 \pm 0.136$	$-0.094 \pm 0.221$	$0.243 \pm 0.077$
count+Nm (SBI)	$0.312 \pm 0.012$	$0.823 \pm 0.019$	$3.472 \pm 0.066$	$1.697 \pm 0.048$	$-0.049 \pm 0.093$	$0.215 \pm 0.049$
count-masked (SBI)	$0.330 \pm 0.061$	$0.842 \pm 0.062$	$3.417 \pm 0.172$	$1.694 \pm 0.099$	$-0.049 \pm 0.219$	$0.217 \pm 0.054$
log10m (SBI)	$0.330 \pm 0.059$	$0.871 \pm 0.041$	$3.530 \pm 0.061$	$1.732 \pm 0.047$	$0.055 \pm 0.083$	$0.197 \pm 0.048$
count+log10m masked (SBI)	$0.310 \pm 0.012$	$0.829 \pm 0.019$	$3.441 \pm 0.065$	$1.677 \pm 0.047$	$-0.077 \pm 0.094$	$0.237 \pm 0.044$
count+Nm with selection bias fixed (SBI)	$0.317 \pm 0.011$	$0.816 \pm 0.015$	$3.491 \pm 0.055$	$1.713 \pm 0.040$	$-0.013 \pm 0.075$	$0.202 \pm 0.043$
count+Nm with free selection bias (SBI)	$0.317 \pm 0.011$	$0.817 \pm 0.019$	$3.489 \pm 0.062$	$1.708 \pm 0.043$	$-0.017 \pm 0.084$	$0.203 \pm 0.045$
count+Nm (SBI, one sim.)	$0.320 \pm 0.013$	$0.822 \pm 0.020$	$3.451 \pm 0.071$	$1.701 \pm 0.051$	$-0.058 \pm 0.098$	$0.231 \pm 0.049$
count+Nm (SBI:TK10, Flagship)	$0.307 \pm 0.013$	$0.807 \pm 0.019$	$3.482 \pm 0.069$	$1.737 \pm 0.050$	$-0.078 \pm 0.099$	$0.206 \pm 0.052$
count+Nm (SBI:TK08, Flagship)	$0.308 \pm 0.015$	$0.831 \pm 0.025$	$3.434 \pm 0.083$	$1.670 \pm 0.062$	$-0.084 \pm 0.122$	$0.240 \pm 0.055$
count (analytic likelihood)	$0.327 \pm 0.048$	$0.824 \pm 0.048$	$3.459 \pm 0.141$	$1.710 \pm 0.083$	$-0.012 \pm 0.180$	$0.212 \pm 0.058$
log10m (analytic likelihood)	$0.320 \pm 0.072$	$0.823 \pm 0.055$	$3.496 \pm 0.057$	$1.721 \pm 0.044$	$-0.002 \pm 0.082$	$0.204 \pm 0.047$
count+log10m (analytic likelihood)	$0.316 \pm 0.008$	$0.816 \pm 0.012$	$3.490 \pm 0.044$	$1.713 \pm 0.032$	$-0.012 \pm 0.062$	$0.206 \pm 0.033$